RICE UNIVERSITY

Charge Transport and Transfer at the Nanoscale Between Metals and Novel Conjugated Materials
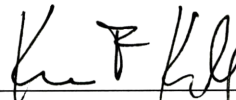
by

Jeffrey Howard Worne

A Thesis Submitted
in Partial Fulfillment of the
Requirements for the Degree
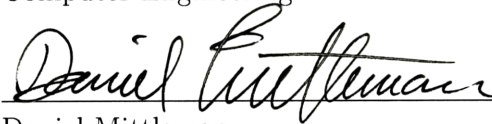
Doctor of Philosophy

Approved, Thesis Committee:

Douglas Natelson, Chair
Professor of Physics and Astronomy

Kevin F. Kelly
Associate Professor of Electrical and
Computer Engineering

Daniel Mittleman
Professor of Electrical and Computer
Engineering

Houston, Texas

April, 2012

ABSTRACT

Charge Transport and Transfer at the Nanoscale Between Metals and Novel
Conjugated Materials

by

Jeffrey Howard Worne

Organic semiconductors (OSCs) and graphene are two classes of conjugated ma-
terials that hold promise to create flexible electronic displays, high speed transistors,
and low-cost solar cells. Crucial to understanding the behavior of these materials
is understanding the effects metallic contacts have on the local charge environment.
Additionally, characterizing the charge carrier transport behavior within these mate-
rials sheds light on the physical mechanisms behind transport. The first part of this
thesis examines the origin of the low-temperature, high electric field transport behav-
ior of OSCs. Two chemically distinct OSCs are used, poly-3(hexylthiophene) (P3HT)
and 6,13- bis(triisopropyl-silylethynyl) (TIPS) pentacene. Several models explaining
the low-temperature behavior are presented, with one using the Tomonaga-Luttinger
liquid (TLL) insulator-to-metal transition model and one using a field-emission hop-
ping model. While the TLL model is only valid for 1-dimensional systems, it is
shown to work for both P3HT (1D) and TIPS-pentacene (2D), suggesting the TLL
model is not an appropriate description of these systems. Instead, a cross-over from
thermally-activated hopping to field-emission hopping is shown to explain the data
well. The second part of this thesis focuses on the interaction between gold and
platinum contacts and graphene using suspended graphene over sub-100 nanometer

channels. Contacts to graphene can strongly dominate charge transport and mobility as well as significantly modify the charge environment local to the contacts. Platinum electrodes are discovered to be strong dopants to graphene at short length scales while gold electrodes do not have the same effect. By increasing the separation distance between the electrodes, this discrepancy is shown to disappear, suggesting an upper limit on charge diffusion from the contacts. Finally, this thesis will discuss a novel technique to observe the high-frequency behavior in OSCs using two microwave sources and an organic transistor as a mixer. A theoretical model motivating this technique is presented which suggests the possibility of retrieving gigahertz charge transport phenomena at kilohertz detection frequencies. The current state of the project is presented and discrepancies between devices made with gold and platinum electrodes measured in the GHz regime are discussed.

Acknowledgments

So many people have helped me reach this point that a simple page or two of thanks cannot possibly capture my level of gratitude. But, I'm going to do what I can. I should note that the order of this list is quite arbitrary, as my thanks should all be presented simultaneously. Unfortunately, that would make a rather incomprehensible document, so due to the limitations of the written word, a list will have to suffice.

First, I'd like to thank my doctoral adviser, Doug. Doug is the kind of adviser everyone in graduate school should want to have. He is exceedingly patient, an excellent teacher, and his passion for physics is infectious. He will be hands-on when you need him to be, but also knows when he needs to let you have your space to discover or learn on your own. Because of this, Doug has made me a better writer and scientist. To Doug goes my deepest thanks... this would not have been possible without you. Thank you.

Second, my parents... thank you so much for your tireless support and encouragement, even if you didn't understand my work (which, by the way, is my fault for not explaining it better). I felt your pride and happiness when I would tell you about a publication or conference I was presenting at, and I always got a kick when Dad would google me looking for the latest reference of my goings-on. Thank you too for springing for flights home when I couldn't afford it and for coming to my aid when I needed surgery. And beyond the obvious biological fact that this wouldn't have been possible without you, this really wouldn't have been possible without you. Thank you.

To my sister, Colleen... I've been so proud of you and your dedication to pursue science as a career. You have no idea how happy that makes me! I've enjoyed seeing

you grow as a scientist and as a woman, and I'm very impressed. Thank you for being a bad-ass [insert 'me gusta' face here - will that even make sense when this gets read in the future?].

I'd also like to thank my extended family, who have been very supportive during my time at Rice and have shown great interest in the work I have been doing. Not attending family functions has been hard, but being able to see you all at least once a year is always good. Unfortunately, my living situation keeps me in Texas, but I hope to be able to see you at least twice a year.

Next, I'd like to thank my labmates, both past and present. Aaron, Jaylin, Behrang, Zach, and Dan... you guys made work a pleasurable experience. I appreciated our discussions about physics, politics, video games and the random garbage that I found on the internet. I'm pleased to have known each of you and look forward to visiting you all in the future (except Jay... dude, you're in Korea after all!) to discuss our glory days in the Natelson lab. The rest of the labmates - Kenny, Jenny, Heng, Ruoyu, Patrick, Joey, Jiang, and Will... thank you for being excellent coworkers and good friends. You have made the Natelson lab an exceptional place and, honestly, the best lab on campus. You should feel proud and lucky that you're all an integral part of that process. Thank you.

Thank you also to Angelo and Tim. I always enjoy our lunchtime discussions and you have both been exceptional friends throughout the years. I'm looking forward to keeping in touch with you both. Maybe one of these days I'll treat Angelo to a ride to a restaurant. Seriously, I probably owe you $1000 in gas money.

To my California posse (Mike, Jenn, Stephanie, Steve, Jesse), thanks for being such great friends throughout the years. I always look forward to hanging out with you when I'm able to make it back to SoCal. In-N-Out and Cinni-middles! I think it's high time that you guys visit Texas. Seriously. To my Houston crew (you know who you are), I'm excited that I get to spend more time with you. This whole grad school experience would have been quite boring and uninspiring without you.

A shout-out needs to be given to my fur-ball of a cat, Harvey. Despite the hairballs, you're a cute little dude and have been a great companion. You may not be able to read, but I think you'd agree.

And, finally, to Laura Jones. This last part is bittersweet, given the current nature of our relationship. I cannot possibly capture our years together in a couple sentences, nor can I possibly communicate how lucky I was to have you tap me on my shoulder. You were my biggest fan, closest ally, best banterer, and best friend. Thank you for introducing me to 'Noles football, Jazzfest, *Friends* and *Project Runway*, NOLA, and Summa. Thank you for teaching me to stick up for myself, to manage my time better, and to be a better person. Getting a Ph.D. is one thing, but knowing you and loving you truly justified my time spent in graduate school. I wish our geographic situation was different, but we're both career-minded individuals that want nothing else but to succeed... unfortunately that has placed us in different parts of the country. I am truly sorry for the pain I put you through; there is no one least deserving of that than you. I don't know if our paths will cross again, but if they did, I'd be sure to tap you on your shoulder.

Contents

Illustrations

Chapter 1

Introduction

This introduction will cover material to acquaint the reader with the basic physics behind organic semiconductors and graphene. This is by no means a complete treatment of the physics behind these materials; rather it is to get the reader quickly acquainted with the basic ideas governing their properties. The first section will address organic semiconductors, their history, and the physics of their operation. The second section will address graphene, its history, and its basic physics. Finally, this chapter will end with an outline to the remainder of this thesis.

1.1 Organic Semiconductors

Organic semiconductors (OSCs) are poised to become the *de facto* material of choice to solve a wide-variety of engineering problems not yet possible with current silicon-based technologies. The driving force behind commercial research is on display technology. In the past several years, the theoretical consumer applications of organic semiconductors have recently begun to be realized, with flexible prototype cell phones and transparent displays. Figure 1.1 shows two prototypes recently displayed by Samsung in 2011. The future technology is focused on developing OSC-based radio-frequency identification (RFID) tags [9] and low-cost OSC-based photovoltaic solar cells[10]. The marketplace for OSCs is strongly dominated by its niche placement as a low-cost alternative to silicon. Due to the low carrier mobility in OSCs, however, they will not replace silicon-based electronics for high-speed computation.

The beginnings of modern day organic semiconductor research began with McGinness, *et al.*, who made what is widely considered the first electrical switch using
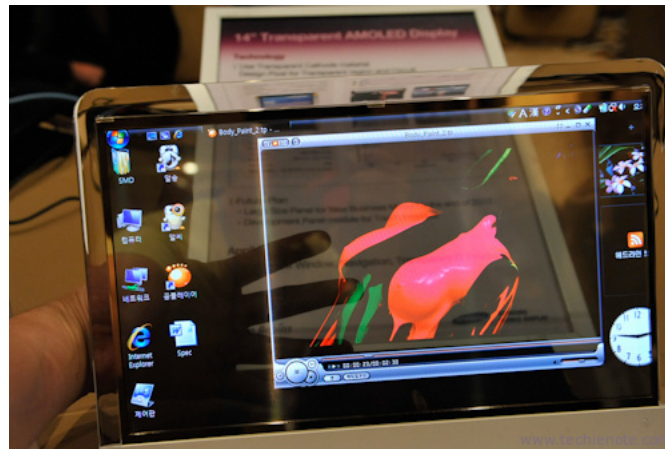
(a)

(b)

Figure 1.1 : (a) A transparent display based on active matrix organic light-emitting diode technology (ref. [1]) and (b) small, hand-held displays designed to illustrate future cell phone technology (ref. [2]). Both are developed by Samsung.

melanin as the active layer[11]. Three years later, Shirakawa, *et al.*, developed the first doped polyacetylene films, thereby turning a plastic "insulator" into a conducting polymer[12]. For this work, Hideki Shirakawa, Alan MacDiarmid, and Alan Heeger were awarded the Nobel Prize in Chemistry in 2000. As soon as this seminal paper was published, it was clear that a new branch of chemistry had been born.

Today a wide range of molecules are available for organic-based devices. Organic semiconductors offer a fairly tunable bandgap through the range of visible light. They can be rigid, crystalline, and highly conductive or soft, amorphous, and flexible. They can be solution processed, printed out using ink-jet technology, and are fairly non-toxic. The wide range of potential applications also yields a fruitful testbed of study, offering an experimental framework to examine percolation theory and charge transport in disordered systems [13, 14, 15, 16, 17]. Ultimately, with success already shown and future potential virtually assured, organic semiconductors will reach a state of ubiquity similar to that of Kleenex, the Rubix cube, or quantum mechanics [18].

1.1.1 Charge Transport in Organic Semiconductors

A modest tutorial on charge transport will be presented here. For a very thorough treatment, refer to references [19] and [20]. It is first instructive to discuss what is meant by charge mobility, as this is an important metric in device performance which describes the underlying physical phenomena in OSCs. Then, various charge transport models will be presented based on electron-phonon coupling and transport through a disordered network.

1.1.1.1 Mobility

Mobility can be defined as the local diffusion of a charge carrier about an average position[19], described by the Einstein-Smoluchowski equation,

$$\mu = \frac{eD}{k_B T},$$ (1.1)

where μ is the mobility, e is the electron charge, D is the diffusion constant, k_B is the Boltzmann constant, and T is temperature. With equation 1.1, no external electric field is applied. In practice, this method of determining mobility is not straightforward. Instead, if mobility is defined as the drift of the average position under applied electric field, one obtains the following equation,

$$\mu = \frac{v_d}{E},$$ (1.2)

where v_d is the drift velocity and E is the applied electric field. Using time-of-flight measurements, one can obtain the mobility by simply measuring the average time it takes for charges to move from one electrode to the other. Typical values for mobility in OSCs are less than 1 cm^2/V·s [21], whereas mobilities in silicon can be three orders of magnitude higher.

Many factors influence charge carrier mobility. In order to efficiently move charge, it is important to improve charge movement between molecular chains, to reduce disorder within the semiconducting film, and to reduce charged traps and impurities. Mobility in organic semiconductors is also strongly dependent on electric field and temperature, as discussed in chapter 2. All of these features give plenty of experimental "knobs" to adjust in order to elucidate the charge transport properties of OSCs. OSC molecules have significant anisotropy in mobility, in both the intra-molecular [5] and inter-molecular [22] directions. This suggests that ordering on the molecular scale is important. OSCs develop their charge transport characteristics through the overlap of p-orbitals between the molecules. The overlapping p-orbitals form π-bonds

and delocalized π-electrons. If a sufficient number of π-bonds overlap, the delocalization of electrons increases. Therefore, one route to increasing mobility is to improve the π-bond overlap, thereby improving charge carrier movement between molecules [23]. Polymers that are engineered to stack in ways that increase their π-bond overlap are termed regioregular. Improvement in π-bond overlap can be done for small molecules as well, generally leading to a crystalline microstructure[24]and a herringbone packing geometry. More information about regioregularity will be covered in section 1.1.2.

Intimately connected to improving π-bond overlap is the reduction of disorder within the OSC film. Two types of disorder are present in these systems, diagonal disorder and off-diagonal disorder. Diagonal disorder refers to the fluctuation in energy of the individual molecular or polymer chains, whereas off-diagonal disorder refers to disorder between neighboring molecules or chains[19]. Both forms of disorder serve to modify the highest-occupied molecular orbital (HOMO) and lowest-unoccupied molecular orbital (LUMO) (analogous to valence and conduction bands in inorganic semiconductors). The HOMO and LUMO levels become Gaussian broadened due to the disorder, with widths on the order of 50-100 meV[25, 26].

Disorder can manifest itself through energetic traps and grain boundaries that inhibit charge carrier motion. Energetic traps remove charge carriers from the OSC, thereby reducing the overall mobility. Using the multiple trapping and release model[27], with homogeneously distributed traps, the mobility is expressed as

$$\mu = \mu_0 \alpha \exp\left(-E_t/k_B T\right), \tag{1.3}$$

where μ_0 is the trap-free mobility, E_t is the energy of the trapping site, and α is the ratio of density of states for charge carriers to density of traps. Work done by Horowitz and Hajlaoui [28] have shown that grain boundaries dominate the trap sites, modeled as back-to-back Schottky barriers. Based on this model, equation 1.3 suggests that mobility is thermally activated and gate-voltage dependent, as higher temperatures

make it easier for charges to overcome the Schottky barrier, and larger gate voltages can lower the Schottky barrier height. This equation is similar to the Arrhenius law describing thermally-activated hopping transport between disordered sites,

$$\mu \propto \exp\left(-\Delta/k_B T\right), \tag{1.4}$$

where Δ is the activation energy required to hop (which is acquired thermally), increasing with more disorder. As temperature decreases, these disordered systems evolve to a temperature-independent mobility where charge carriers tunnel across the grain boundaries[28]. Additional information about the high- and low-temperature descriptions of mobility is discussed in chapter 2. This mobility behavior is in contrast to crystalline, band-like transport, which shows a

$$\mu \propto T^{-n} \; n = 0.5 - 3 \tag{1.5}$$

temperature-mobility relationship. This behavior has been observed in single-crystal rubrene [29] and tetracene [30] through, among other techniques, time-of-flight measurements [31].

1.1.1.2 Charge Transport

Charge transport in organic semiconductors is strongly dominated by dynamic and static factors. The dynamic factors are generally categorized as electron-phonon interactions that are modified as temperature is changed. As mentioned above, mobility of these materials is strongly temperature dependent, and can be categorized as the sum of the hopping and tunneling contributions [19]

$$\mu = \mu_{tunneling} + \mu_{hopping}. \tag{1.6}$$

The first term represents the mobility at low-temperatures characterized by tunneling across grain boundaries, and the second term represents the thermally-activated hopping behavior at high temperatures. As the temperature is varied, contributions from both tunneling and hopping behavior contribute to the overall measured mobility. Based on the strength of the local electron-phonon (e-p) coupling, several modes of transport behavior are observed. For weak e-p coupling, mobility is band-like, and is proportional to temperature as shown in equation 1.5 for all temperatures. For stronger local e-p coupling, band-like transport occurs at very low temperatures. As temperature is increased, thermally activated hopping begins to dominate coupled with the formation of polarons. A polaron is a composite quasiparticle comprising a charge carrier and the deformation of the nearby environment. This deformation originates from the electrostatic interaction between the carrier and its surroundings, similar to a ball bearing distorting a rubber sheet. The depth the ball goes into the sheet represents a larger polaron energy, and if the energy increases further, the charge carrier can become trapped. As temperature increases into the hopping transport regime, molecular degrees of freedom increase as well making available more energies for polaron formation [19]. Higher temperatures therefore increase the effective mass of charge carriers due to the presence of polarons which greatly contributes to the reduction of tunneling mobility and destruction of band-like transport.

The static factors that influence charge transport are related to disorder within the film. As disorder increases, transport bands are narrowed forcing charge carriers to hop between regions of localized transport instead of delocalized movement. Disorder is introduced when the OSC polymer chains and molecules take on random on-site energies selected from a Gaussian distribution. This broadens the HOMO and LUMO levels as mentioned previously, and places charge carriers into the tail states of the Gaussian distribution [19]. Instead of modeling mobility as a function of trapping energy as shown in equation 1.3, Bässler shows [13] that mobility can be modeled as

a function of disorder,

$$\mu \propto \mu_0 \exp\left(\frac{-T_0}{T}\right)^2, \tag{1.7}$$

where T_0 is a function of the disorder present in the film. This enables the measurement of mobility to be a tool in determining the level of disorder present in an OSC system. Disorder caused by localization of the band states therefore serves to reduce mobility, so systems like P3HT that are characterized by hopping between polymer chains are well-described by equation 1.7 at high temperatures $(T > 200K)$.

1.1.2   Molecular Structure

A variety of molecules have been synthesized for use as organic semiconductors. They typically fall into two classes - solution processable polymers like poly-3(hexylthiophene) (P3HT), poly(2,5-bis(3-tetradecylthiophen-2-yl)thieno[3,2-b]thiophene) (PBTTT) and other thiophene derivatives, and small molecules typically processed in vacuum like pentacene or rubrene. Recent advances in synthetic chemistry have developed solution processable small molecules such as 6,13- bis(triisopropyl-silylethynyl) (TIPS) pentacene[32]. This shares the benefits of wet chemistry with the added increase in device performance. Figure 1.2 shows a representative sample of organic molecules.

The differing chemical structures give rise to various material properties. Because of the long, conjugated backbone found in P3HT and PBTTT, devices made from these materials can undergo substantial mechanical deformation before damaged. With this flexibility, however, comes higher film disorder and lower charge carrier mobility. In order to improve the mobility, P3HT and other thiophene-based materials have regular ordering of their repeating units. Pictured in figure 1.2 (a) is regioregular head-tail P3HT. This ordering of the individual P3HT units improves π-band overlap between neighboring polymer chains, aiding in the delocalization of charge carriers. Crystalline materials like rubrene and, to some extent pentacene, are rigid and inflexible. However, due to their long range ordering, they can exhibit high mobilities (in excess of 15 cm^2/V·s for rubrene [33]) and band-like transport.
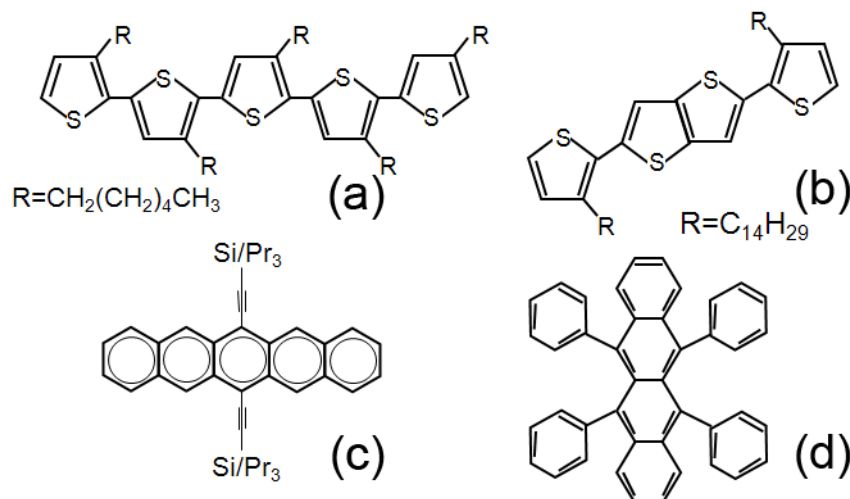
Figure 1.2 : Molecular structure of (a) P3HT, (b) PBTTT, (c) TIPS-pentacene, and (d) rubrene. From (a) to (d), crystallinity, mobility, and rigidity all increase. Single crystal rubrene has shown mobilities in excess of 15 cm^2/V·s, whereas typical mobilities for (a)-(c) lie in the range of 0.1-1 cm^2/V·s.

1.1.3 Charge Injection at the Metal-Organic Interface (MOI)

Equally important to mobility on overall OSC performance is charge injection from contacts into the OSC. In order to make a macroscopic device, contact must be made to it through the application of metallic electrodes. These electrodes will interact with the OSC and, due to energetic differences between the metal and OSC, various interactions will result. Understanding the physical principles behind this interaction is crucial to optimizing OSC performance and to developing a complete theoretical model of these materials. For a thorough treatment of this topic, see reference [9].

Due to the intimate contact required between the metal electrode and the OSC, any surface contamination can serve to alter the MOI. This can be done by changing the electrode work function with surface adsorbates [34] or self-assembled monolayers on the metal surface [35, 36, 37]. Additionally, contact electrodes can dramatically increase the local charge density in the OSC through spontaneous charge transfer [38]. Other experiments looking at charge transfer at the MOI have been performed using

electric force microscopy[39, 40], showing that charge density at the MOI is strongly dependent on electric field. These experiments highlight the sensitivity of the MOI to its local (electrical and chemical) environment and illustrate that important physics is occurring at the smallest of length scales.

To understand this interface, the first attempt made was to apply the Schottky-Mott model originally used for inorganic semiconductors. In this model, the vacuum levels of the metal and semiconductor are first aligned. Due to differences in the relative chemical potentials, charge flow occurs until the chemical potential is equal across the interface. This results in an interface dipole - essentially a voltage potential that exists at the interface due to a non-equilibrium distribution of immobile charged ions and mobile charge carriers. The measured height of the barrier is then, simply, the difference in work function between the metal contact and the electron affinity of the semiconductor [41]. Experimentally, however, it was noted that the choice of metal work function did not influence the value of the interface dipole as predicted by this simple equation. Metals with over a 1eV change in work function had the same interface dipole value. It was later discovered that surface states exist within the band gap of inorganic semiconductors that serve to pin the Fermi level[41], preventing it from equilibrating to an arbitrary value. A convenient metric to measure the quality of the interface is given by

$$S = d\phi_{semi,sub}/d\phi_{sub}, \tag{1.8}$$

where $\phi_{semi,sub}$ is the work function of the semiconductor on the metallic contact and ϕ_{sub} is the work function of the substrate (usually in vacuum). If $S = 1$, complete vacuum level alignment is achieved and little charge is transported across the interface. If $S = 0$, charge transfer occurs. For inorganic semiconductors, $0 < S < 1$.

Analyzing the buried organic semiconductor MOI has proven to be challenging [42], but like their inorganic counterparts, energy band alignment at the MOI was found to differ significantly from theoretical predictions [43, 44]. The common tools used are ultraviolet photoemission spectroscopy (UPS) and x-ray photoemission spec-
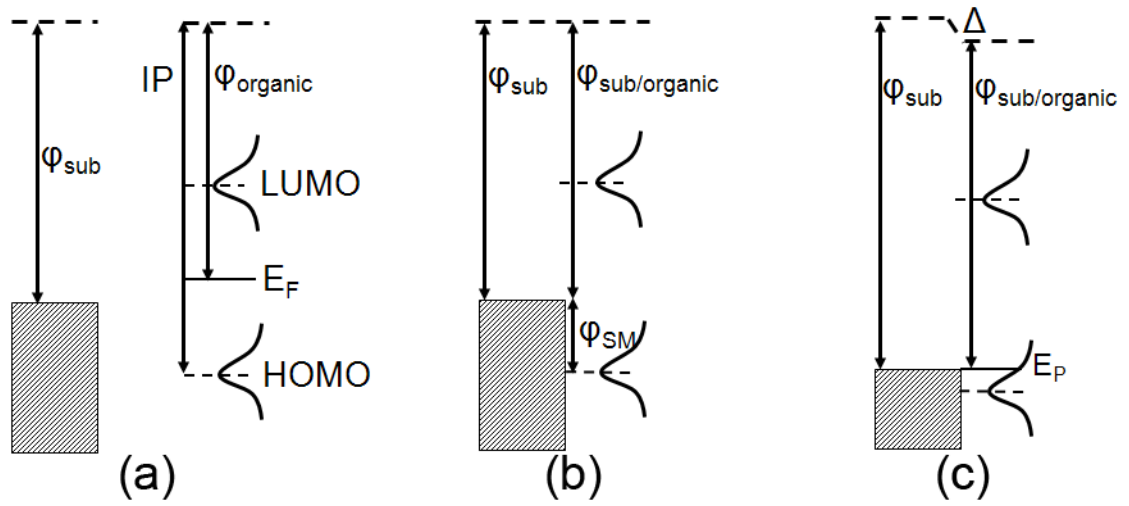
Figure 1.3 : In (a), no contact exists between the metal and the OSC. Gaussian disorder has broadened the HOMO and LUMO levels. In (b), the OSC and metal are in contact, but no charge transfer occurs. The work function of the metal is above the polaron formation energy, and there are no available energy states in the gap. This is the Schottky-Mott limit. In (c), the work function of the contact is equal to or greater than the polaron formation energy, but the measured value of $\phi_{sub/organic}$ is the same. The Fermi level is pinned at the polaron formation energy, E_P in the polymer.

troscopy (XPS), which can probe the buried interface and have shown the error in assuming vacuum level alignment with organic semiconductors and metals [45, 46]. UPS and XPS measurements can also give information about the metal work function, ionization potential of the OSC, and the work function of the OSC on the metal. Recent work [47, 43, 48, 46] has categorized a large number of organic semiconductor/metal interactions and investigated the MOI using UPS. Two distinct regimes of interaction occur. Figure 1.3 illustrates these two regimes.

Initially, the metal and OSC are not in contact, and have vacuum level alignment. This is depicted in figure 1.3(a). In that figure, ϕ_{sub} is the work function of the substrate, IP is the ionization potential of the OSC, E_F is the Fermi level of the OSC, $\phi_{organic}$ is the work function of the organic semiconductor, HOMO is the highest-occupied molecular orbital (similar to the valence band) and LUMO is the

lowest-unoccupied molecular orbital (similar to the conduction band). The bands are energetically broadened to a Gaussian shape due to disorder in the film.

The first regime of interaction occurs when ϕ_{sub} is less (greater) than the polaron formation energy of holes (electrons) in the OSC, shown in figure 1.3(b). In this case, when these materials are brought into contact, traditional Schottky-Mott vacuum level alignment occurs and no charge transfer is thought to occur [46]. This gives an energetic barrier to injection, labeled ϕ_{SM} in the figure. As ϕ_{sub} increases (decreases), so too will the work function of the composite metal/OSC system ($\phi_{sub/organic}$) up until the polaron formation energy for holes (electrons). This gives an S parameter value of 1, indicative of Schottky-Mott behavior.

As the work function of the substrate increases (decreases) for p-type (n-type) OSCs beyond the polaron formation energy, charge transfer occurs at the MOI and an interface dipole (Δ) is established, shown in figure 1.3(c). This also pins the Fermi level of the metal/OSC at the polaron formation energy. Thus, further adjusting the value of ϕ_{sub} will not change the value of $\phi_{sub/organic}$. This behavior suggests that the density of states available for charge transfer are highly localized around the polaron formation energy [47, 46]. As the value of $\phi_{sub/organic}$ remains constant, the S parameter becomes zero. Further adjustment of the metal work function to higher (lower) values does not continue to improve hole (electron) injection. When $S = 0$, the contact is essentially transparent to charge injection, with carriers easily passing from the metal hundreds of nanometers into the bulk OSC. This kind of contact is often called "Ohmic", though it is possible to have a linear relationship between current and voltage across contacts even when there is not perfect alignment between the Fermi level of the metal and the center of the valence or conduction band of the OSC [49, 38].
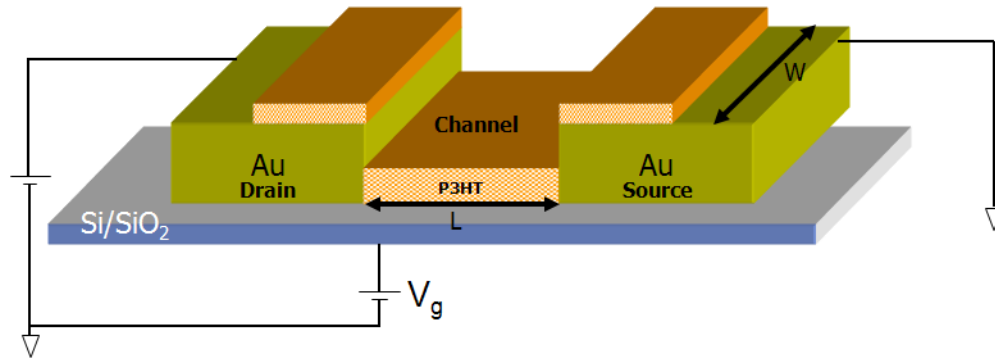
Figure 1.4 : A cartoon illustration (not to scale) of an organic field-effect transistor (FET). Charge is injected into the source electrode, through the organic material and extracted at the drain electrode. The electrodes are fabricated on top of a silicon wafer with silicon dioxide on top that serves as an insulating layer. The wafer also acts as the gate electrode. L is the length, and is defined to be the inter-electrode distance measured along the channel. W is the width of the channel, or linear distance of the electrode parallel to the channel.

1.1.4 Transistor Description and Modes of Operation

A field-effect transistor (FET) is nominally a three-terminal device consisting of source electrode, drain electrode, and gate electrode. The space between the source and drain is termed the channel. For a p-type FET, the source electrode is where charge is injected and the drain electrode is where charge is extracted (and is, therefore, ground). The electrodes themselves are interchangeable, however, as source can be come drain and *vice versa* depending on the bias applied. The gate electrode is usually a highly-doped wafer of silicon with a thermally grown oxide on its surface, which serves as an insulator. This wafer also serves as the substrate for device fabrication. W and L define the width and length of the active region of the transistor; width is measured parallel to the channel and length is the inter-electrode distance. Devices with high aspect ratio have a large W/L ratio, and are featured in this thesis. A cartoon depicting the structure of an organic FET is shown in figure 1.4.

Fabricated devices look quite different than the cartoon, but the majority of the difference comes from the need for large contact pads. Figure 1.5 is an optical mi-
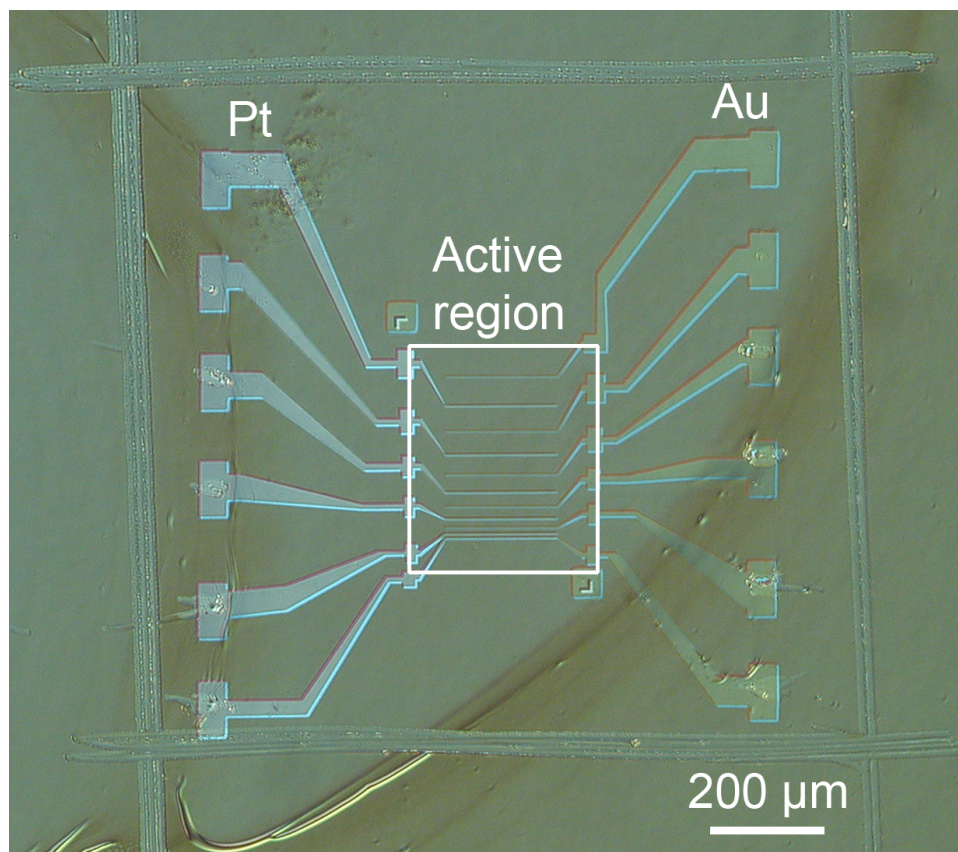
Figure 1.5 : A microscope image of a representative organic FET. The left is platinum (Pt) electrodes and the right is gold (Au) electrodes. The region highlighted in the middle is the active region, where the majority of charge transport occurs. Because the P3HT is a continuous film, conduction happens through all parts, but is concentrated in the active region. The box around the electrode group is made using a probe tip to isolate this device from the gate electrode, preventing current leakage through the gate.

croscope image of a typical device. In the figure, Pt and Au electrodes are pictured, as well as the active region of the transistor. Current can flow throughout the entire P3HT film, but it is concentrated in the active region of the FET device. Discolorations in the image are areas of thicker P3HT film, and are usually areas of higher disorder and lower mobility. Typically, the best OSC measurements are made when there are no film discolorations over the active region of the device.

Transistors usually operate in two modes, the linear regime and the saturation

regime. By applying a gate voltage, charge carriers are attracted to the gate interface. This creates an accumulation of charge carriers, creating a low resistance channel and allowing current to flow from the source to the drain. Provided $V_S < V_G - V_T$, the transistor will be in the linear regime. Assuming the drain electrode is ground, current is characterized by

$$I_S = \mu C_{ox} \frac{W}{L} \left[(V_G - V_T) V_S - \frac{V_S^2}{2} \right], \tag{1.9}$$

where I_S is the current measured in the channel, μ is the device mobility, C_{ox} is the capacitance per unit area of the gate oxide, V_G is the gate voltage, V_T is the threshold (turn-on) voltage, and V_S is the voltage applied across the channel. As source voltage increases, the device begins to enter saturation. Saturation occurs when the region near the source electrode is pinched off to a region of intrinsic resistance due to the local electrostatics. The cross-over from the linear regime to the saturation regime occurs when $V_S \geq V_G - V_T$, with the equation for current in the saturation regime given by

$$I_S = \frac{1}{2} \mu C_{ox} \frac{W}{L} (V_G - V_T)^2 \tag{1.10}$$

Note the lack of dependence on V_S in equation 1.10. For a more complete treatment on transistors and their modes of operation, as well as when these equations break down, refer to reference [41].

1.2   Graphene

Graphene is a 2-dimensional allotrope of carbon, with atoms arranged in a hexagonal lattice. Graphene is the 2-dimensional building block of graphite, where individual layers of graphene are weakly bonded to each other through van der Waals forces. It can be obtained using several methods, some of which are outlined in section 3.2. According to both theory and experiment, truly two-dimensional materials are impossible [50, 51], as two-dimensional crystals are not thermodynamically stable. Graphene overcomes this obstacle by developing nanometer-scale corrugations on its
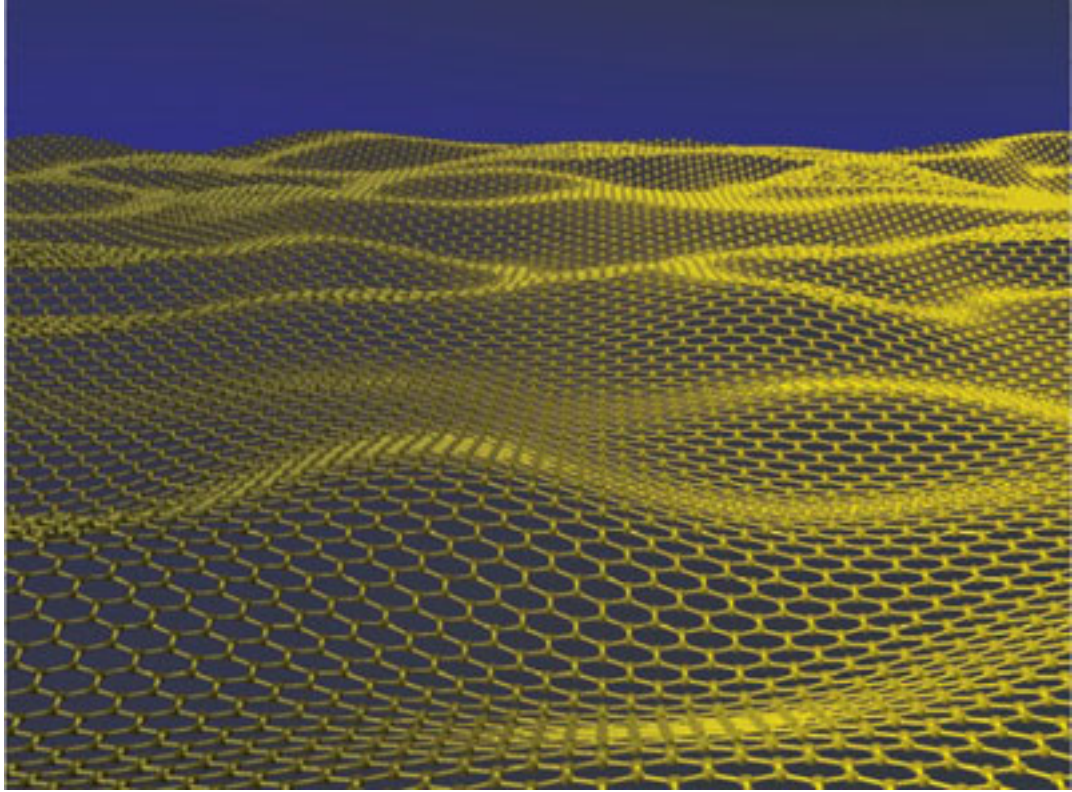
Figure 1.6 : Artists depiction of graphene. Note the hexagonal lattice structure and the multiple peaks and valleys. Adapted from ref. [3].

surface [52]. A brief outline of the properties of graphene will be presented here. A more thorough treatment can be found in chapter 3 and in reference [53]. An artists depiction of graphene is shown in figure 1.6.

1.2.1 Band Structure and Charge Transport

Graphene is part of a class of materials (like topological insulators [54]) with unique electronic structure properties. Unlike topological insulators, whose surface states are metallic but its bulk is insulating, graphene is a 2-dimensional, atomically thick material. The band structure in graphene can be described by the Dirac Hamiltonian, a direct result of the long-range ordering found in the material [55]. As a consequence, charge carriers within graphene have zero rest-mass and can approach Fermi velocities

on the order of $c/300$. In addition, due to the long-range order, scattering sites are minimized and mobilities can reach upwards of 200,000 cm^2/V·s [56]. The lack of disorder also enables charge carriers to travel several hundred nanometers before scattering, possibly enabling future devices with zero resistance and very low power consumption.

The band structure near the equilibrium chemical potential is linear, and is described by the energy relation, $E = \hbar v_f k$, where $\hbar$ is the Dirac constant, v_f is the Fermi velocity and k is the charge carrier momentum. Near the crossing of the Fermi energy, termed the Dirac point, the density of states goes to zero, indicating there should be zero charge transport. Experimentally[57, 58], however, the minimum conductivity at this point has been found to be $\sim e^2/h$, with such small spread in data that it suggests this value may be quantized [55]. The origin of the minimum conductivity still remains somewhat of a mystery, but current experimental evidence points to the formation of charge puddles (both hole and electron) in the graphene sheet, possibly due to impurities or structural disorder [59, 60].

Disorder also plays a role in the edge states of graphene. Edge states are artificial, controllable regions of disorder, providing a good testbed for investigating the effects of disorder on transport. Two types of edges are possible, armchair or zig-zag. These names are derived from the crystal lattice direction within graphene chosen to define the edge. Both edge states are metallic, but only the zig-zag edge has zero-energy modes at non-zero momentum values[53]. Graphene nanoribbons also allow for the creation of a band-gap. If the nanoribbon is narrow enough to where the edge states begin to dominate, the 2-dimensional nature will be reduced to 1-dimensional particle-in-a-box behavior through quantum confinement [61]. Additionally, grain boundaries and edge states provide the necessary disorder for inter-valley scattering of charge carriers, leading to the observation of weak localization at low temperature [62].

1.3   This Thesis

This thesis primarily deals with novel conjugated materials - organic semiconductors and graphene - and their nanoscale interaction with metals. In chapter 2, the high-temperature and low-temperature behavior of P3HT and TIPS-pentacene is investigated. Comparison to the theory presented in section 1.1.1 is made, and data illustrating the transition from thermally activated hopping transport to field-emission hopping transport are presented. Additionally, several claims of an insulator-to-metal transition are discussed, but evidence contrary to these hypotheses is shown.

In chapter 3, a different type of conjugated material is presented, along with a novel engineering solution to create nanoscale ($\sim$50 nm) suspended graphene transistors. Both gold and platinum electrodes are brought into intimate contact with graphene in order to probe the charge transfer that occurs at the graphene/metal interface. Data that suggests high amounts of hole-doping for platinum contacts but not for gold contacts are shown, manifest though a shift of the minimum conductivity point to a positive gate voltage. As the electrode separation distance increases to the micron scale, evidence of the shift in minimum conductivity disappears, giving an upper bound on the distance of charge diffusion from the contacts.

In chapter 4, a novel probe technique for organic semiconductors is presented. Two detuned microwave sources are injected into an organic FET and, due to the non-linearities present in the FET, the microwave signals are mixed and the low-frequency component is measured. Theory describing the information contained within this low-frequency component is discussed, and the current state of the data and the analysis is shown. The current interpretation of mixing occurring at the metal-organic interface and not within the organic FET is discussed, and the need for additional theory to explain the data is mentioned.

Chapter 2

Transport in Organic Semiconductors in Large Electric Fields: From Thermal Activation to Field Emission

2.1 Introduction

Understanding the high electric field behavior of organic semiconductors is important in organic light-emitting diodes, organic field-effect transistors and organic photovoltaics. Frequently, large fields are required in order to get organic FETs to enter the saturation region and large fields make charge collection more efficient in photovoltaics. Much of the recent effort in studying this behavior has come from the influence large electric fields have on the charge injection process[42, 39, 63]. The high electric field behavior of the bulk has been similarly analyzed, and transport is typically described as a combination of space charge effects and mobility modified by the local electric field [25, 21, 64, 65]. In general, the mobility of organic semiconductors is dependent on temperature, charge carrier density, electric field and film disorder[20], with reason to believe that appropriate descriptions of room temperature behavior do not work at low temperatures [64].

The room temperature behavior of organic semiconductors has been well described by the Poole-Frenkel (PF) model of mobility[13, 66], valid over a certain electric field and temperature range. Within this range, the PF mobility can be described by the following equation

$$\mu_{PF} = \mu_0(T, V_G) \exp(\gamma\sqrt{E}). \tag{2.1}$$

where μ_0 is the zero-field mobility (dependent on temperature and gate voltage), E is the electric field and γ is a term related to the hopping mechanism present (i.e. thermal activation)[21]. Both μ_0 and γ have been found to vary like $1/T$ when equation 2.1 is valid [25, 21, 65].

Outside this range, mobility tends to increase with decreasing electric field and follows a $\mu \propto E^{-1}$ behavior for increasing electric field [13]. This is generally considered a consequence of disorder present in the organic film. As outlined by Bassler [13], at low electric fields, hopping paths that are more energetically favorable (but require more hopping events) can have the charge carrier travel against the applied electric field. In low fields, the charge carrier can take this path, but as the field increases, the charge carrier is restricted in its ability to move in this direction. This causes a decrease in mobility with increasing field. As these low fields are insufficient to alter the energetic barriers that make certain, perhaps more direct, paths unfavorable to transport, mobility continues to decline. Once the field reaches a certain threshold, however, these barriers are lowered, and an increase in mobility with electric field strength is seen, which follows equation 2.1. Increasing the electric field further yields a decrease in mobility as charge carriers do not have enough time to hop out of a particular site to allow room for additional charge carriers to occupy that site. This is effectively space-limited charge transport, where the space-charge is altering the local electric field preventing additional charge carriers from traveling with the field.

The Poole-Frenkel model is only valid for temperatures where hopping transport dominates. As the temperature is decreased, strong deviations from equation 2.1 are noted [21], as transport becomes highly non-linear and temperature independent with $T \rightarrow 0K$. Several theories exist as to the origin of this change from the PF mobility regime to this non-linear regime. Under the influence of high electric fields and low temperatures, Dhoot *et al.* argue that the organic semiconductor undergoes a voltage-driven insulator-to-metal transition[67]. As T decreases, they note that the transport behavior initially trends toward the conductivity, σ, going to zero - exactly

as insulators behave. However, as T decreases further and approaches some critical value, σ becomes constant with decreasing temperature provided a large gate and source-drain bias are applied. Similar to Dhoot, *et al.*, Yuen, *et al.*, argue[5] that as T goes from 300K to 4K, polymer organic semiconductors undergo a insulator-to-metal transition that is described by the Tomonaga-Luttinger liquid (TLL) model. The TLL model has found success in describing truly one-dimensional systems like nanotubes and one-dimensional wires[68, 69], but had not yet been invoked to describe organic semiconductor behavior.

Other theories suggest that the organic semiconductor undergoes a crossover from a thermally activated (PF) hopping regime to a field emission (FE) hopping regime[70][71, 72]. This viewpoint is further supported by the multistep tunneling process.[73] In this process, under high gate and source-drain bias, tunneling of charge carriers occurs through the existence of randomly distributed local states within the organic film. This provides a modification to the mobility, where μ_{PF} becomes

$$\mu_{FE} \propto \mu_0 \exp(-\sqrt{E_0/E}) \tag{2.2}$$

where $E_0(V_G)$ is temperature independent and is expected to depend on the disorder in the sample[70], and E is the average electric field in the transistor channel. The crossover point to go fully from activated hopping to field emission hopping is dependent on the applied electric field and the strength of charge localization[70]. This theory is in contrast with Dhoot, *et al.*, and Yuen, *et al.* whose argument lies in an insulator-to-metal transition and not a modification to the mobility.

As outlined in the introduction to this thesis, organic semiconductors have a variety of chemical structures that define their electronic behavior. Molecules like poly-3(hexylthiophene) (P3HT) used in this thesis or poly(2,5-bis(3-tetradecylthiophen-2-yl)thieno[3,2-b]thiophene) (PBTTT) used by Yuen, *et al.*, have mobilities along the chain axis that are several orders of magnitude greater than the mobility in the π-stacking direction[5]. Consequently, these materials could be considered 1-
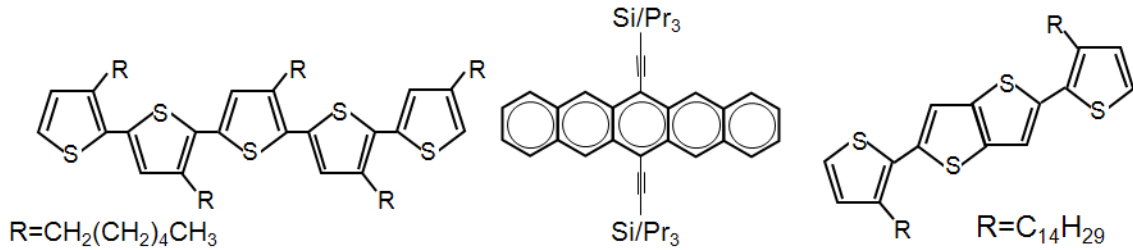
Figure 2.1 : Molecular structure of poly-3(hexylthiophene) (P3HT) [left], 6,13- bis(triisopropyl-silylethynyl) (TIPS) pentacene [middle], and poly(2,5-bis(3-tetradecylthiophen-2-yl)thieno[3,2-b]thiophene) (PBTTT) [right]. P3HT and PBTTT have similar molecular structures, and these structures above are repeated many times to build up long chains. These chains lie in a glassy, disordered matrix. Both P3HT and PBTTT could be considered 1-dimensional. TIPS-pentacene, on the other hand, forms molecular crystals and can only be described as 2-dimensional.

dimensional conductors and be potentially described by the TLL model. These organic semiconductors create films that are glassy on the macroscale with nanoscale regions of order. It is within these ordered regions that the TLL model would apply.

However, molecules like 6,13- bis(triisopropyl-silylethynyl) (TIPS) pentacene[32] are short chain molecules without orders of magnitude anisotropy in mobility. Some anisotropy has been measured[22], but electronic structure calculations of this molecule do not indicate that it is 1-dimensional in nature[74]. TIPS-pentacene tends to form van der Waals bonded molecular crystals that assist in creating a 2-dimensional system. Because of its 2-dimensional nature, TIPS-pentacene should not show any TLL-like behavior. This will become important later in this chapter as the voracity of the TLL model is analyzed. As a reference, the molecular structure of these molecules (P3HT[75], TIPS-pentacene[32], PBTTT[76]) is presented in figure 2.1.

When the temperature is decreased in the P3HT and TIPS-pentacene systems, this chapter will show that charge transport evolves from the PF-style activated hopping at high temperatures to field-emission hopping at low temperatures. Additionally, this chapter will show that while the use of the TLL model as a fit to the data for both P3HT and TIPS-pentacene looks valid, this analysis seems unsatisfying. The

1-dimensional nature of P3HT and PBTTT is still under debate, but it is clear from a molecular perspective that TIPS-pentacene cannot be considered 1-dimensional and, therefore, cannot be described by TLL physics.

This section of the thesis will therefore deal with analyzing the TLL claim for P3HT and TIPS-pentacene, and whether it makes sense to describe the low-temperature and high electric field behavior of P3HT as an insulator-to-metal transition. Additionally, a simpler model for transport at low-temperature and high electric field will be presented that models both the behavior of P3HT and TIPS-pentacene without the need for invoking exotic physical models.

2.2 Sample Fabrication and Experimental Setup

Samples were fabricated on degenerately-doped p-type silicon wafers with 200 nanometers of thermally grown oxide. This served as both the gate and the substrate for these experiments. Platinum electrodes were fabricated using standard electron-beam lithography techniques, electron-beam metal deposition, and lift-off processing using acetone. Platinum was chosen as the contact metal because it provides the lowest barrier to injection in organic materials[38, 77]. Device A (P3HT as active layer) had a channel width, W, of 50 μm and channel length,L, of 300 nm. Device B (TIPS-pentacene) had a $W = 200$ μm and a $L = 1$ μm. In addition, other electrodes of varying channel length were included on the substrate to provide a testbed to measure contact resistance and mobility using the transmission line technique[21]. In all cases, electrode thickness was 15 nm with a 1 nm Ti adhesion layer. Electrodes were rinsed in acetone and isopropanol and were then cleaned in oxygen plasma for two minutes. An SEM micrograph of the fabricated electrodes is shown in figure 2.2. Following this, samples were spin-coated with hexamethyldisilazane (HMDS) at 3000 rpm for 30 seconds, followed by a bake at 130°C for 20 minutes. The HMDS treatment serves to passivate the silicon oxide so that dangling bonds and energetic traps do not effect charge transport within the organic semiconductor.

A

RICE   SEI   15.0kV   X37   100µm   WD 10.1mm

127nm

B

RICE   SEI   15.0kV   X30,000   100nm   WD 10.3mm
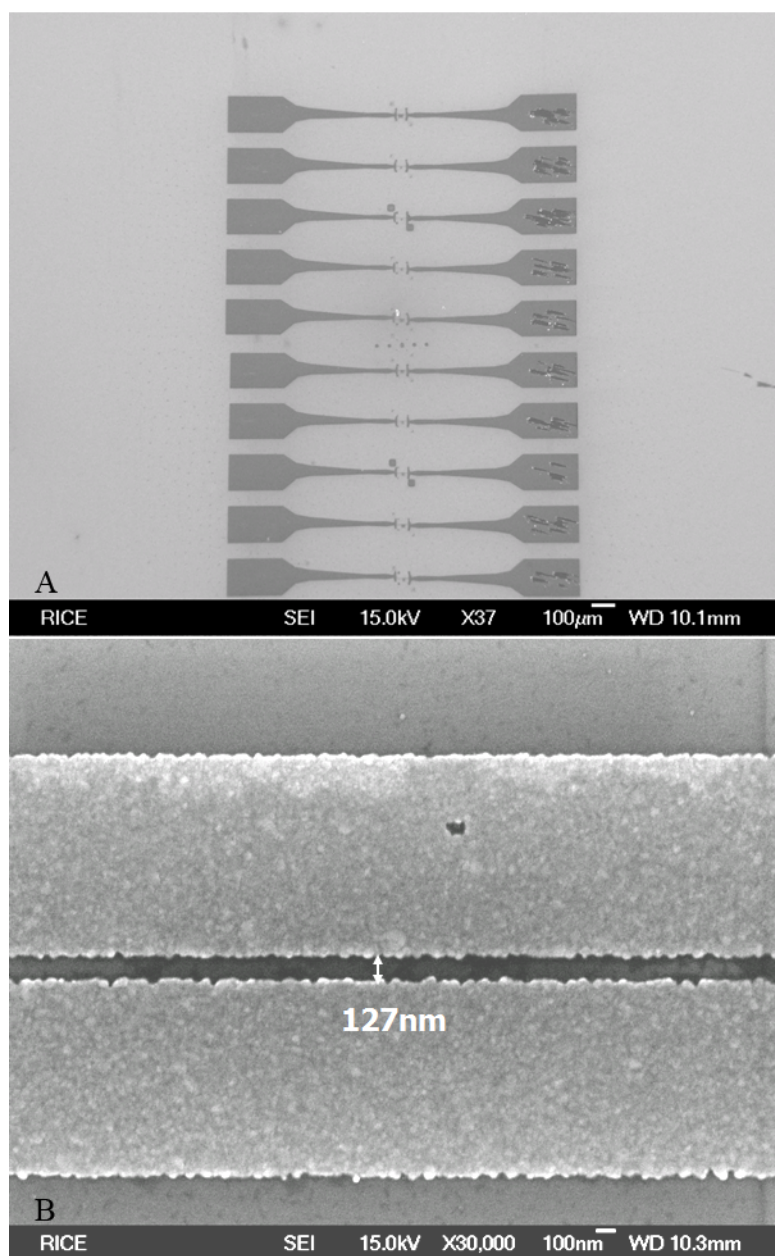
Figure 2.2 : SEM micrograph of fabricated electrodes. The scale bars present are 100 µm in (A) and 100 nm in (B). The direction of the arrow in (B) indicates the channel length (the vertical direction), and the horizontal direction indicates channel width.

P3HT was spin-cast from chloroform at a 0.1% by weight concentration (15 mg P3HT in 15 mL of chloroform) onto device A. TIPS-pentacene was drop cast from toluene at a 1% by weight concentration onto device B. Samples were measured in a variable temperature probe station with base pressure of $\sim 10^{-6}$ Torr. Samples were then heated to 375K for 12h in order to remove water and oxygen dopants so that the intrinsic properties of these materials could be studied. In order to isolate the devices from each other and from the gate electrode, a probe tip was used to remove the organic semiconductor in a rectangle around the device being tested. Temperature was varied from 300K to 4K in increasingly finer steps as $T \rightarrow$ 0K. Transport measurements were conducted using a Hewlett Packard HP4145B, with ambient light blocked from entering the probe station to avoid photoexcitation of the P3HT and TIPS-pentacene.

In order to characterize the films, transmission line measurements were made in order to determine the mobilities and contact resistances of the P3HT and TIPS-pentacene devices. The transmission line measurement technique is outlined in the introduction to this thesis. The mobility for P3HT was determined to be 4.6×10^{-2} cm^2/V·s and the mobility for TIPS-pentacene was determined to be 1.1×10^{-4} cm^2/V·s. The mobility of the P3HT film lies well within values reported in literature[21, 38], but the mobility for TIPS-pentacene was anomalously low. This low mobility can be attributed to poor crystal uniformity and a large number of grain boundaries between crystal regions. This should not change the overall results, however, as charge transport within the TIPS-pentacene crystal grains is unaffected by poor morphology. Further, TIPS-pentacene remains a 2-dimensional material regardless of the quality of the films.

Contact resistances were also extracted from the devices and were compared to bulk resistances. Bulk resistances were at least an order of magnitude larger than the contact resistances, indicating that these devices are bulk dominated. Additionally, based on previous work[21], as temperature is reduced, contact resistance values

increase more slowly than the bulk resistance, effectively making contact resistances decrease relative to the bulk with decreasing temperature. Therefore, the devices remain bulk dominated down to the lowest temperatures. Source-drain voltage values were chosen so that the electric field within the channel was consistent between Device A and Device B. For device A, the maximum electric field was 20MV/m, and in device B it was 10MV/m.

2.3 Poole-Frenkel Model of Transport

The P3HT and TIPS-pentacene devices were first checked to see if they could be described using the PF model shown in equation 2.1. They were measured from 300K down to 210K for device A and from 285K to 195K for device B. Then, the data was fit to the following equation with the form[65]

$$I_D = \frac{\mu_0 w C_i}{L} \exp\left(\gamma \sqrt{V_{DS}/L}\right) \left[(V_g - V_T))V - \frac{V_{DS}^2}{2} \right], \quad (2.3)$$

where μ_0 and γ are defined above for equation 2.1 and are used as fitting parameters, C_i is the capacitance per unit area of the gate oxide, and V_T is the threshold voltage for the transistor. The highest gate voltage used, $V_g = -80V$ was used for the analysis in order to have the highest currents available as the device was cooled. The results of the fitting and the high temperature dependence of source-drain current versus source-drain bias are shown in figure 2.3. The inset of figure 2.3a shows the device geometry and the relevant descriptors of the device (W, L, source, drain and gate). The value for γ is larger in the TIPS-pentacene case than for the P3HT case, indicating that the nature of the localized states differs between P3HT and TIPS-pentacene[21], likely due to greater disorder in the pentacene film. The greater disorder is also reflected in the poorer mobilities for the TIPS-pentacene films. As T decreases, the PF model begins to deviate from the data, indicating a cross-over into the field emission hopping regime. This is not the true cross-over point, however. Rather, as T approaches 200K,

(a)

(b)
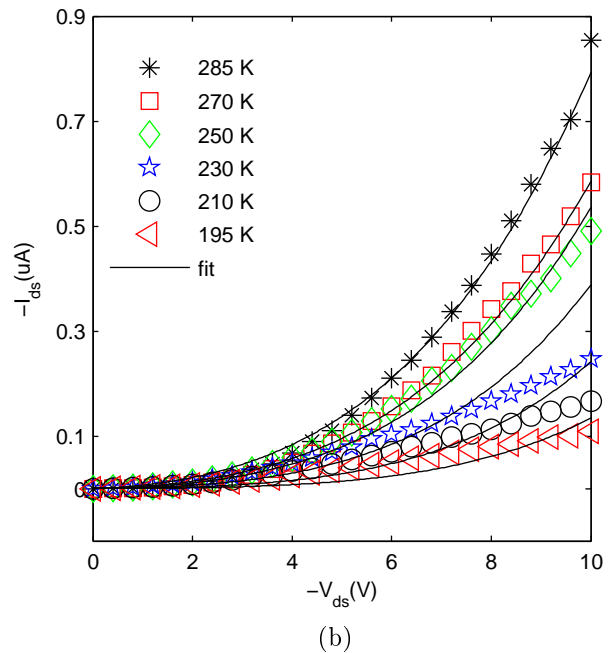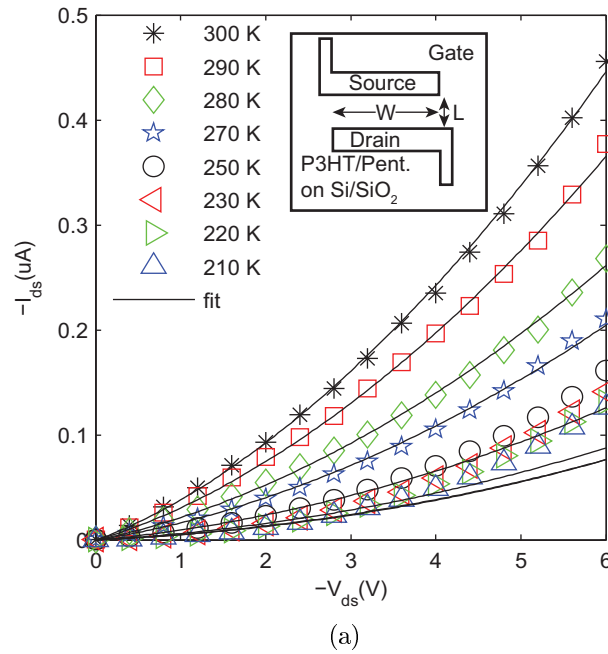
Figure 2.3 : $I_{DS} - V_{DS}$ curves for device A (P3HT) and device B (TIPS-pentacene) over a 100K temperature range for $V_G = -80V$. Fit lines are derived from a Poole-Frenkel field dependence of the mobility from equation 2.3. The deviation of the fit lines from the measured data indicates the beginning of the cross-over from the Poole-Frenkel regime to the field emission hopping regime. The inset in figure 2.3a describes the device geometry. Adapted from reference [4]
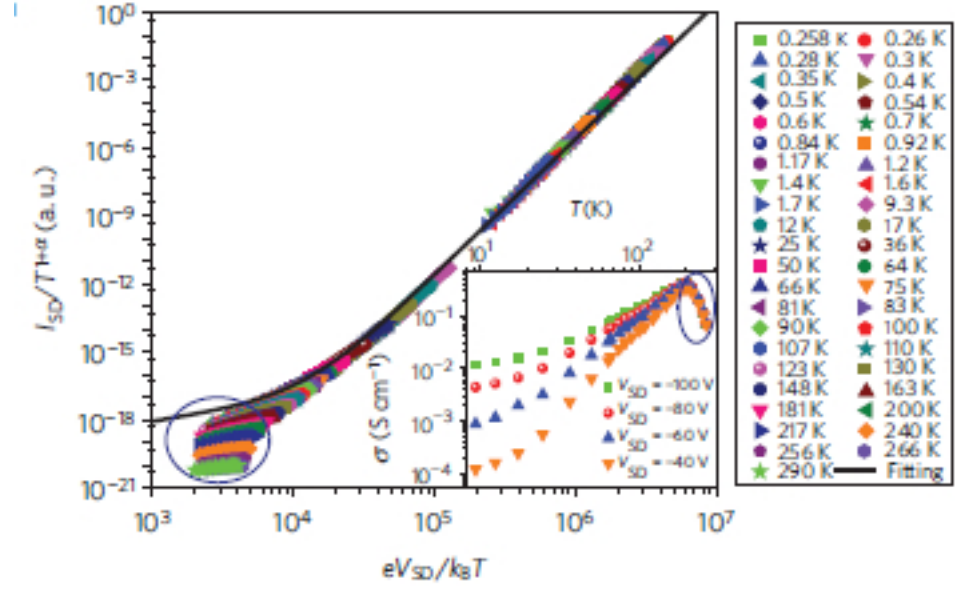
Figure 2.4 : Data presented by Yuen, *et al.* in reference [5]. It is essentially an $I_{SD} - V_{SD}$ plot with temperature scaling in both the x-axis and y-axis. In addition, data has the ability to be scaled along the y-axis depending on the choice of α.

transport is likely a mix of PF and FE.

2.4 Analysis of the validity of the Tomonaga-Luttinger Liquid theory for organic semiconductors

Once the P3HT and TIPS-pentacene films were verified to follow the PF model, they were then analyzed using the method suggested by Yuen, *et al.* Their data plot results are shown in figure 2.4. One important note is the nature of the axes in figure 2.4. The axes are both scaled by $1/T$, and data along the y-axis can be scaled through the use of α. This will be shown to artificially produce the TLL physics shown here.

The expression for the current represented by the fit line is[68, 5]

$$I = I_0 T^{\alpha+1} \sinh\left(\gamma' eV/k_B T\right) |\Gamma\left((1+\beta)/2 + iV/\pi k_B T\right)|^2, \qquad (2.4)$$

where Γ is the Gamma function, α and β are phenomenological constants estimated from plots of conductance versus T and $I(V)$, respectively, and γ' is a phenomenological parameter thought to relate to the amount of disorder (i.e. tunneling barriers) present in the 1-dimensional structure. The plotting, as shown in figure 2.4 is done in the following manner. At fixed V_G, one plots $I_D/T^{\alpha+1}$ versus (eV_{DS}/k_BT) with α as the fit parameter. With a properly chosen α, the fit line generated in equation 2.4 will collapse onto all of the data, thus implying that the TLL model describes the behavior of the system. As previously stated, however, even though P3HT and PBTTT may be regarded as 1-dimensional systems, TIPS-pentacene cannot be. Therefore, there should be no expectation of TLL behavior in TIPS-pentacene.

Following the technique outlined above, the P3HT and TIPS-pentacene data was plotted, shown in figure 2.5. With appropriate choices of α (5.43 for P3HT and 7.1 for TIPS-pentacene), it is possible to collapse the fit line from equation 2.4 onto the data. These values for α are not very different from those reported for PBTTT[5] (5.4, 4.3) or polyaniline fibers[78] (2.2-7.2). Therefore, the systems both seem to fit the criteria for being described by the TLL model, despite the previous arguments against this for TIPS-pentacene.

So, if TIPS-pentacene cannot be described by TLL physics, how is a plot similar to the data for P3HT and PBTTT obtained? The danger in this style of analysis lies in several areas. As T decreases, conduction in organic semiconductors becomes non-linear (as shown in figure 2.6) and becomes temperature independent. Because the choice of plotted voltage range is narrow, choosing these roughly power-law shaped curves and plotting them on log-log axes makes these data appear to be straight lines. The freedom to then choose an arbitrary α value in the y-axis allows for continuous adjustment until the data points lie on a straight line. Furthermore, the scaling in the x- and y-axis which both have a $1/T$ dependence will shift data up and to the right with decreasing T. This will occur even if the actual data points do not change with temperature at all. As a consequence, plotting data in this manner leaves too many
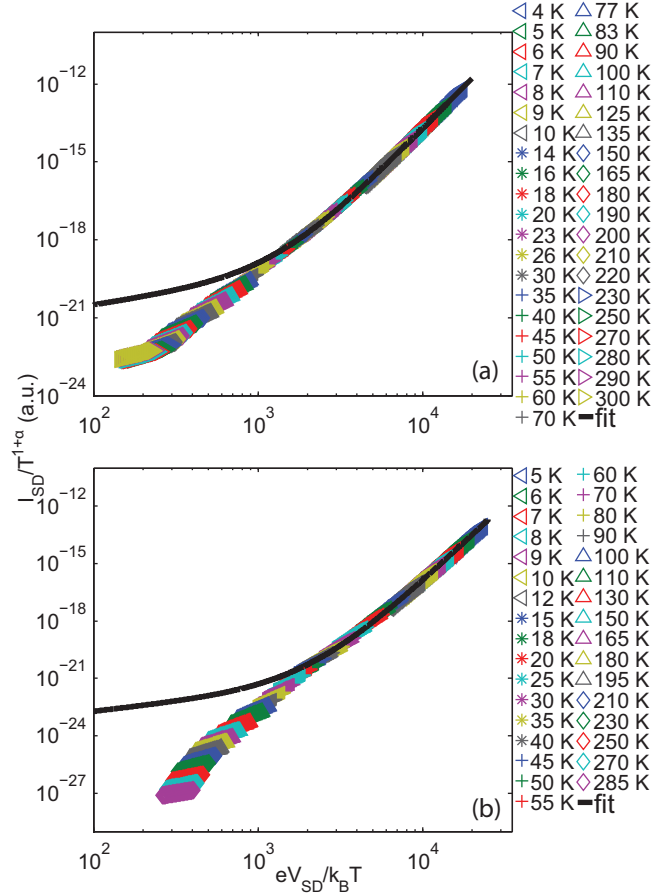
Figure 2.5 : Plot of I_{SD} versus V_{SD} as suggested by Yuen, *et al.* using eq. 2.4 to generate the fit lines (solid). The top figure, (a), is the P3HT device ($V_G = -80V$) and the bottom figure, (b), is the TIPS-pentacene device ($V_G = -70V$). For device A, $\alpha = 5.43$ and $\gamma' = 4 \times 10^{-3}$; for device B, $\alpha = 7.1$ and $\gamma' = 3 \times 10^{-3}$. For both fits, the relation $\beta = \alpha + 1$ was used. The correspondence between the fit line and the data is a consequence of the method used to plot the data and the nature of the low-temperature I-V curves. It does not suggest that TLL physics describe the behavior of these materials. Adapted from reference [4]

free parameters that do not reflect the true nature of the behavior of these materials. Therefore, this is not a convincing method to determine that TLL physics is at work in organic semiconductors.

2.5 Field emission hopping model for low-temperature and high electric field

As shown above, despite the convincing nature of figures 2.4 and 2.5, the TLL model cannot be applied. Instead, it is proposed that charge transport evolves from thermally-driven activation hopping to field emission hopping, as outlined in equation 2.2. Equation 2.3 is then modified to become

$$I_D = \frac{\mu_0 w C_i}{L} \exp\left(-\sqrt{E_0/\left(V_{DS}/L\right)}\right) \left[\left(V_g - V_T\right) V_{DS} - \frac{V_{DS}^2}{2}\right]. \qquad (2.5)$$

Taking the data from the lowest temperature $I_{DS} - V_{DS}$ curves, they are fit to the equation 2.5, shown in figure 2.6. The quality of the fit suggests that the model described by equation 2.5 is valid. This suggests that both P3HT and TIPS-pentacene transition to a field emission hopping regime as $T \to 0K$. In addition, the data are fit well by a temperature independent μ_0 (0.3 for P3HT and 9 for TIPS-pentacene). Further analysis to connect this behavior to the multistep tunneling model[73] presented earlier will require an understanding of the effect of gate voltage on E_0 and truly understanding the origin of the cross-over threshold temperature to go from thermal hopping to field emission hopping.

2.6 Conclusion

The origin of the temperature and electric field behavior of organic semiconductors has been studied and debated for quite some time. Several theories present interesting arguments, some with compelling physical explanations. By taking two materials with very different molecular structures, this chapter has shown that models invoking
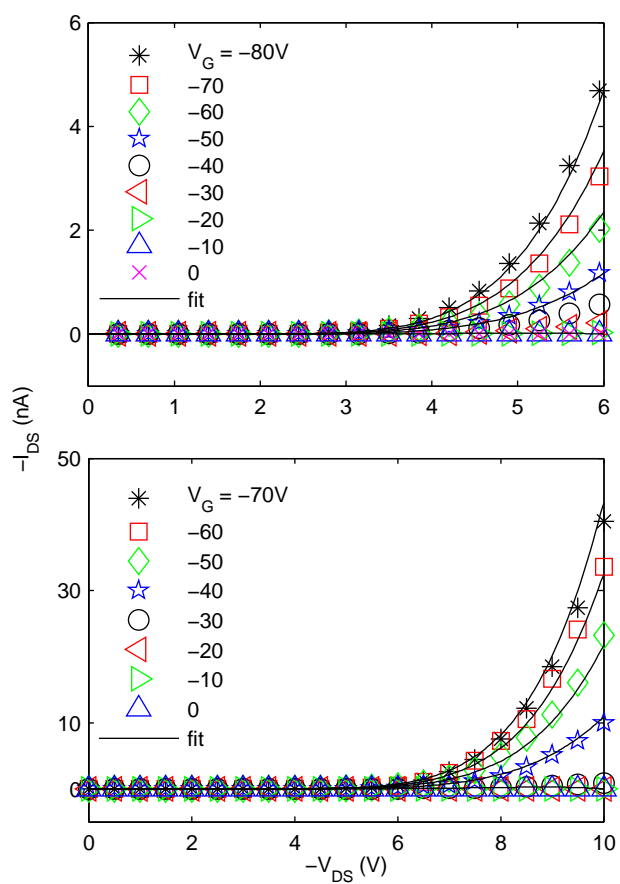
Figure 2.6 : P3HT (a) and TIPS-pentacene (b), measured at 4.2K and 5K respectively. The black lines are the fits derived from equation 2.5. The fit is fairly strong for both P3HT and TIPS-pentacene, suggesting that they both make the transition from thermal hopping to field emission hopping.

the insulator-to-metal transition of 1-dimensional organic semiconductors does not appear to be correct. While P3HT has significant anisotropy in its mobility along the chain axis versus across neighboring chains, claiming TLL physics using the methods outlined above is unwise. Being able to show that TIPS-pentacene, a material with no microscopic basis for TLL physics, can also be modeled in the same way indicates a flaw with the conclusions of Yuen, *et al.*

Instead, data was presented that captures the behavior of both P3HT and TIPS-pentacene over a wide temperature range, encompassing both the high-temperature Poole-Frenkel-like activated hopping behavior and the low-temperature, field emission hopping behavior. This analysis respects the increasingly temperature independent nature of transport in these materials as T is decreased, and incorporates parameters that may have a true physical bearing on the disorder present in the organic films. Further detailed investigations should be able to fully connect these two regimes with an unified model illustrating the full temperature and field dependence, perhaps by purposefully controlling the disorder within these materials.

Chapter 3

Local Charge Doping in Suspended Graphene Nanojunctions

3.1 Introduction

This chapter of the thesis will discuss graphene and the effect metallic contacts have on its local charge environment. As outlined in the introduction in section 1.2, graphene is a truly 2-dimensional material consisting of carbon atoms arranged in a hexagonal lattice structure. Because of its unique band structure and the possibility of preparing large areas of the material, graphene has the potential to be important in electronics[79], photovoltaic devices[80], and other systems[81]. In order to fabricate any of these devices, however, contact must be made to graphene, which typically involves the use of metals. Understanding the interaction between metals and graphene and the charge transfer that occurs at their interface will be crucial in designing future graphitic devices.

In certain cases, charge transfer is seen as undesirable. The dangling bonds present on the surface of SiO_2 can induce charge puddles in graphene and thereby limit charge transport[56, 82]. In fact, interaction energies between graphene and SiO_2 can be on the order of 0.4 meV/^{2}[82]. Isolating graphene from the SiO_2 substrate using boron nitride[83], which has a similar lattice constant to graphene and is chemically inert for the energies of interest within graphene, has recently become popular. This reduces the interaction between graphene and the silicon oxide. Other research uses mica as the substrate, reducing the influence of charged impurities, with the added benefit of an atomically flat substrate[84].

Controlled doping, however, can allow for device engineering by exposing graphene

to reactive metal ions[57] or chemical species,[85, 86] thereby altering graphene's electronic states and making it $n-$ or $p-$type doped. Enabling selective doping in this way allows for the future development of diodes and complementary logic. The influence metal electrodes have on the local charge environment in graphene has also been studied using scanning photocurrent measurements[87, 88, 89] as well as experiments using a 4-probe geometry[90, 91]. The photocurrent studies found that charge carriers from the contacts can diffuse several hundred nanometers into the bulk by noting that areas generating photocurrent were larger than the contact pads. This has also been confirmed theoretically[92].

Despite the ubiquity and importance of metal contacts, their role in graphene charge transport has only recently been explored. The interaction between metals and other carbon-based systems like nanotubes has been well-studied[93, 94, 95] but the treatment given to these materials cannot be applied to graphene, due to its unique band structure. Charge carriers in graphene behave like massless Dirac fermions[58] allowing for suppressed charge screening when in contact with a metal. Poor screening implies that the inhomogeneous electrostatic potential produced by the screening charges is long-ranged, leading to the behavior seen in scanning photocurrent studies. Contacts can lead to marked changes in charge transport and local density of states[8, 92], $p-n$ junctions at the metal-graphene interface[96, 80], charge density fluctuations near the contacts[97], and even the formation of a band-gap[98]. In general, the influence contacts have on graphene is complicated and, as such, has taken some time to be understood both experimentally and theoretically.

Because of the long-range diffusion of charge carriers in graphene, electrical probing of this transfer is possible provided the electrode separation distance is no greater than twice the diffusion length for charge carriers. Depending on the work function of the contacts and the interaction of them with graphene, holes or electrons will diffuse into the channel between the electrodes. This will then manifest itself as a shift in the charge neutrality point (CNP) as graphene is pushed to be either $n-$ or $p-$type

doped. The CNP will shift because of the local charge environment - the contacts transfer additional mobile charge carriers into the channel, and one must then apply a certain gate voltage in order to restore charge neutrality. With sufficient distance from the electrodes, however, the charge density should return to the bulk distribution. Using the technique developed in our lab by A. Fursina, *et al.*, in reference [99], we are able to fabricate suspended graphene transistors with a high aspect ratio - width/length - of ∼300 with channel lengths less than 100 nm. Many of the channel lengths studied are at or below 50 nm. The fabrication process will be covered in more detail in section 3.2.3.

This chapter will discuss the fabrication of suspended graphene transistors as well as the influence contacts have on the charge distribution near the graphene/metal interface. It will show the large shifts in CNP indicative of charge transfer into graphene, but only occurring for certain graphene/metal interfaces. This chapter will also discuss the length dependence of charge injection and conclude with potential applications of this technology.

3.2   Sample Fabrication and Experimental Setup

3.2.1   Exfoliated Graphene

Even though exfoliated graphene is not used in this experiment, it is useful to have the technique outlined here for future reference. While it was widely successful for the original graphitic studies[58], the technique for mechanical exfoliation of materials with strong intra-layer bonds but weak van der Waals inter-layer bonds has been used for quite some time with mica other various materials[51]. The method used for exfoliation reported on in this section was the Scotch tape method. First, highly-ordered pyrolytic graphite (HOPG) is used due to its high quality graphite layers, although Kish graphite is common in the literature. Conventional translucent Scotch-brand tape is used for the exfoliation process. Other types of acetate tape have been used, but their performance was poor compared to the traditional Scotch-brand tape.
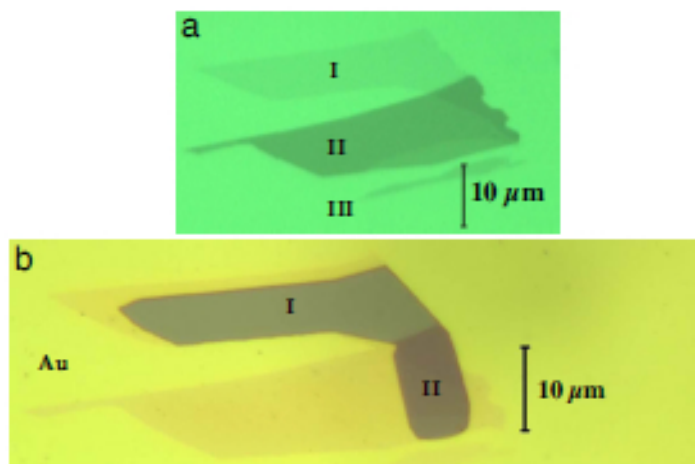
Figure 3.1 : Adapted from reference [6]. In (a), region I is single layer graphene and is just visible over the background of the SiO$_2$. Region II is a bi-layer region. In (b), Au is deposited as a contact electrode.

The exfoliation method is as follows: 1) take a long piece of Scotch tape, roughly 6-8 inches. It is advisable to wear latex gloves in order to limit the contamination of the tape. Fold the ends of the tape over so that there are roughly 1/2 inch areas that are not sticky. 2) Place the middle of the tape onto the HOPG stack, and then gently remove it. This transfers many layers of HOPG to the tape. 3) Fold the tape in half so that both sides of the transferred HOPG are in contact with the tape. 4) Slowly peel the tape apart, leaving two regions with HOPG on the tape. 5) Continue this folding and peeling process until very little is transferred between steps. It may be necessary to transfer a section of HOPG from one piece of tape to another as the original piece fills up with peeled flakes. This transfer process is identical to step 2, except one uses the HOPG on the tape. 6) Once sufficiently peeled, take the region that has been exfoliated the most number of times (or regions nearby) and gently place it onto a clean silicon wafer with 300 nm of oxide. The 300 nm of oxide is important in order to view the graphene in an optical microscope with phase contrast. Figure 3.1 shows a typical optical microscope image with regions of single and multilayer graphene[6]. The important thing to remember when looking for exfoliated graphene is that it

will be difficult to see against the background SiO$_2$ coloring. The most promising single-layer graphene pieces will be the most difficult to observe.

3.2.2 Cleaning procedure for graphene-based devices

Regardless of the method chosen to fabricate graphene-based devices, some residual processing material will be left over. Usually this will be residual tape glue or poly(methyl methacrylate) (PMMA) residue from electron-beam lithography. These materials can cause difficulty in making good contact to graphene flakes or can leave behind charged impurities that can alter the CNP and transport properties. There are two methods that work fairly well to remove this contamination. The first is using a commercial oil-based cleaner like Goo Gone. This is best used for exfoliated graphene with left-over tape glue residue. Simply soak the substrate with graphene in the pure Goo Gone solution for 5 minutes. Rinse in acetone and isopropanol to remove any remaining solution. The down side to this technique is that it can leave behind residue from the cleaner, which is difficult to remove without the use of oxygen plasma or other harsh cleaning methods.

A better removal technique involves using an tube furnace. Place the substrate with graphene into the tube furnace and flow a mix of argon and hydrogen gas; this gas mixture is usually referred to as forming gas. Set the oven to 400°C and let the substrate bake at that temperature for 1 hour. Figure 3.2 shows a before and after image of this technique. Wafers *should* still be cleaned in oxygen plasma, but only *before* depositing graphene. The oxygen plasma will etch graphene, and has been used as an effective patterning technique when coupled with PMMA as a protective over-layer.

3.2.3 Sample Fabrication

Since this experiment did not use exfoliated graphene, degenerately doped $p-$type silicon with 200 nm of thermal oxide was used. This was chosen because of the
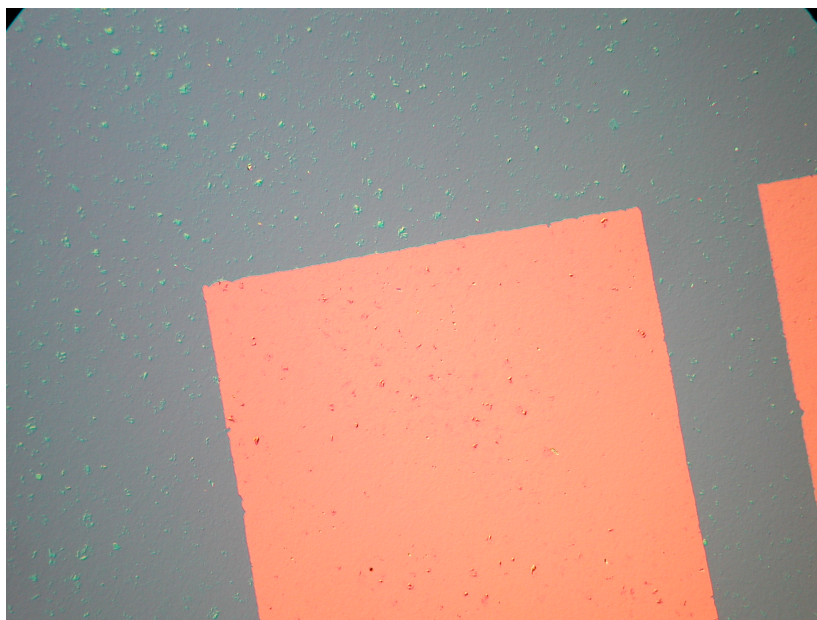
(a)

(b)

Figure 3.2 : Before the cleaning procedure outlined in the text, (a), and after the cleaning procedure (b). The particulates shown in (a) are remnants of the Scotch tape used to transfer exfoliated graphene to the wafer. The remaining material in (b) is transferred graphene with various layer thicknesses.
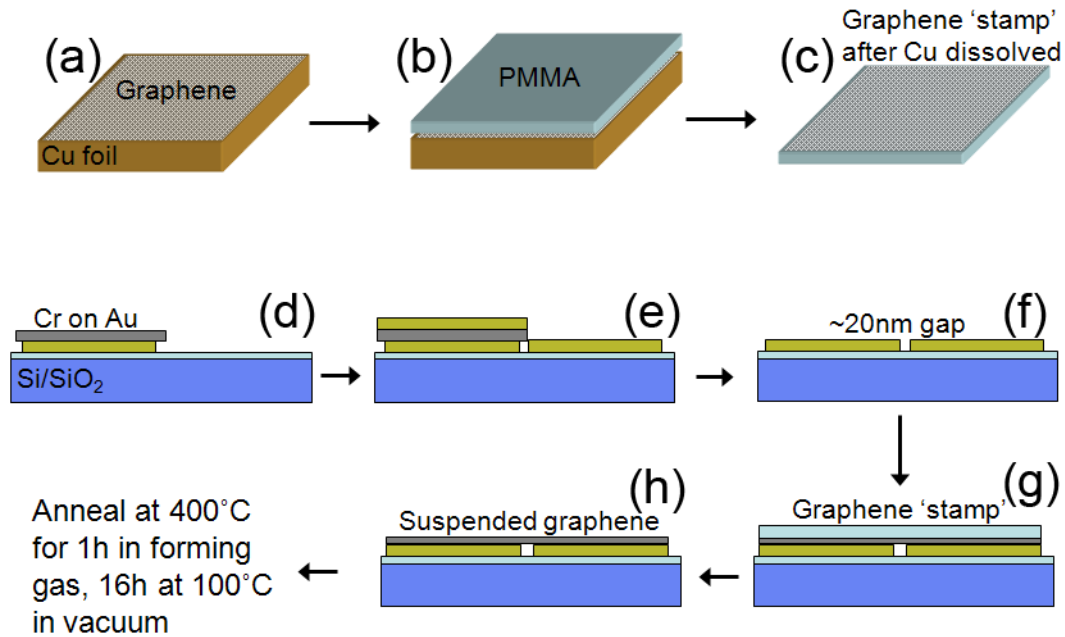
Figure 3.3 : The fabrication process as outlined in the text. (a), graphene is grown via CVD on a copper foil. In (b), PMMA is spun on top of graphene/Cu foil. In (c), Cu foil is etched away leaving graphene on PMMA as a stamp. In (d), lithographically defined electrodes with Ti/Au/Cr are deposited on silicon/SiO$_2$ followed by (e) with a second step of lithography and metal deposition and (f), etching of the Cr layer leaving behind a nanogap. In (g), the graphene stamp is placed on the electrodes and (h) is etched away using acetone. Finally an anneal at 400°C is performed, except for the gold nanogap devices.

familiarity with its processing and the increase in gate coupling between the substrate and graphene. Using two-step electron-beam lithography, electron-beam evaporation, and lift-off processing, electrodes with $w = 20$ μm and average channel length, $l = 51$ nm were fabricated. This technique is outlined in references [100] and [99] but will be covered briefly here. The entire fabrication process is presented in figure 3.3.

Graphene was grown via chemical vapor deposition (CVD) on copper foils (figure 3.3(a)) and a graphene "stamp" is created using PMMA as a transfer medium[100] (figures 3.3(b) and (c)). Next, a set of electrodes is lithographically defined. During evaporation, 1 nm of Ti is used as an adhesion layer, followed by 15 nm of Au or Pt.

Then, 350 nm of Cr is deposited on top of these electrodes (figure 3.3(d)). Gaps on the order of 5 nm can be produced this way using the chromium oxide as a shadow mask, but due to residue from the lithography process, getting the substrate to lie perfectly flat on the roof of the evaporator is difficult. This will impart a tilt to the sample and can generate gaps larger than the oxide thickness. Additionally, the lift-off procedure to remove the Cr layer can be rather harsh, so gap sizes larger than 5 nm should be expected. After stripping the PMMA layer away, a second step of lithography is performed to define electrodes perpendicular to the ones previously made. A second deposition of Ti and Au/Pt is done, this time without a Cr layer (figure 3.3 (e)). The PMMA is stripped and then the Cr layer is etched away (figure 3.3 (f)). The graphene "stamp" from figure 3.3 (c) is then placed on the electrodes and the PMMA is removed using acetone (figures 3.3 (g) and (h)).

The graphene was verified to be single layer through the use of Raman spectroscopy[101]. Based on the images presented in figure 3.4, we believe the graphene to be suspended over the nanogap. Following wrinkles and folds (indicated by arrows in the figure), it looks like graphene is suspended over the gap, as these features do not appear to sag or deviate as they cross from one electrode to the other. In order to compare channel length dependence on charge doping, longer channel length devices ($w = 200$ μm and $l = 1 - 50$ μm) were fabricated using the transmission line approach outlined in chapter 2. These electrodes were similar in composition to the short channel ones, but had no suspended graphene areas.

3.2.4 Device Characterization

Samples were measured in a variable temperature probe station with base pressure of $\sim 10^{-6}$ Torr, and data from 300K to 4K were collected using a Hewlett-Packard 4145B parameter analyzer. Mobilities were calculated[57] by evaluating $d\sigma/dV_G = \mu C_G$ at the largest value of $d\sigma/dV_G$, where C_G is the capacitance per unit area of the gate. Since our graphene is suspended, the serial capacitance model is used to incorporate
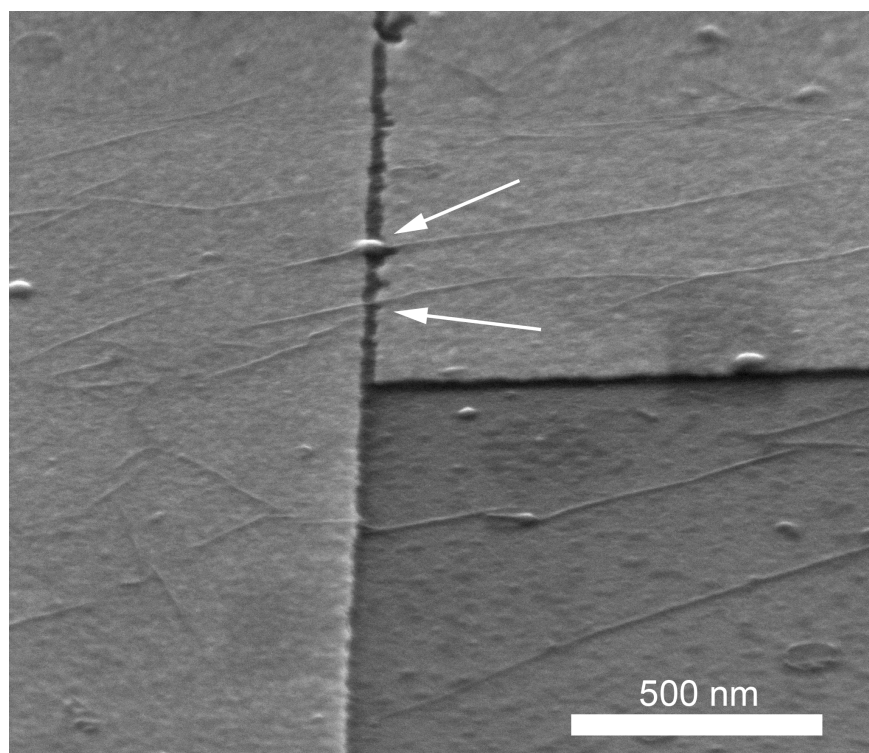
(a)
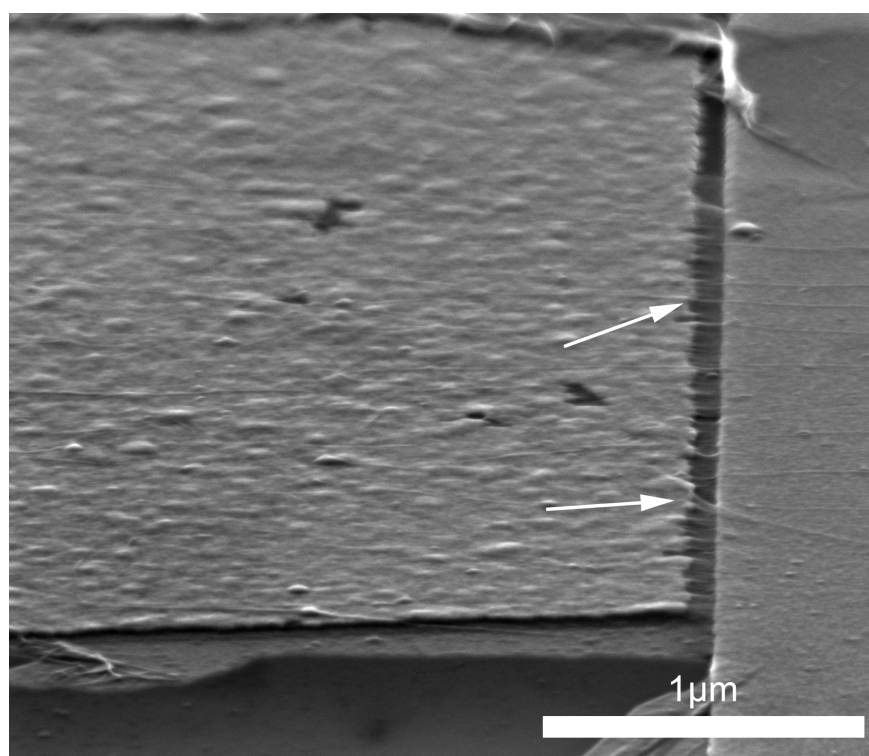
(b)

Figure 3.4 : SEM micrographs of our nanogap devices with graphene on top. Electrode separation in (a) is 52 nm and in (b) 71 nm. Arrows indicate ripples and folds that span the channel suggesting that the graphene is suspended across the nanogap. Thanks to Mark Knight for obtaining these images.

contributions from the gap under the graphene giving $C_G = 7.26 \times 10^{-8}$ F·cm^{-2}. This gap is assumed to be vacuum, however there is likely a monolayer of adsorbed water which could potentially interact with the graphene layer[82]. Fortunately, this monolayer is present in all devices, so its effect should be controlled for. Bias driven self-heating can raise the temperature of the graphene locally[102], but this is only an issue at the lowest temperatures and is unlikely to change the interpretation of the data. For the short channel devices with gold electrodes, $\mu_{20K} = 4.8 \times 10^2$ cm^2/V·s and for the short channel devices with platinum electrodes, $\mu_{20K} = 3 \times 10^1$ cm^2/V·s. The mobility of the interdigitated electrode devices was 3.0×10^3 cm^2/V·s and 1.0×10^3 cm^2/V·s for the gold and platinum devices, respectively. Interestingly, the highest mobilities were found at 20K. This may be due to weak localization effects that manifest because of the low temperature and disordered graphene film, but this is by no means conclusive evidence.

The mobility in these devices is below that which is usually quoted in the literature of $\sim$4000 cm^2/V·s for CVD graphene grown and transferred using similar techniques[100]. This is likely due to defects introduced during the growth and transfer process or by the ripples and folds shown in figure 3.4. Ripples and folds have been found experimentally to increase the resistance in graphene-based devices and limit the mobility of charge carriers[103]. The difference between mobilities in the gold and platinum cases likely arises from differing conditions during the growth or transfer process.

3.3   Local Charge Doping in Suspended Graphene Transistors

3.3.1   Suspended Nanogap Devices

$I_{DS} - V_G$ measurements on the nanogap suspended graphene transistors were taken and are presented in figure 3.5, with data from gold electrodes in figure 3.5(a) and data from platinum electrodes in figure 3.5(b). As presented in the introduction to this chapter, graphene is sensitive to adsorbed species which can alter the local
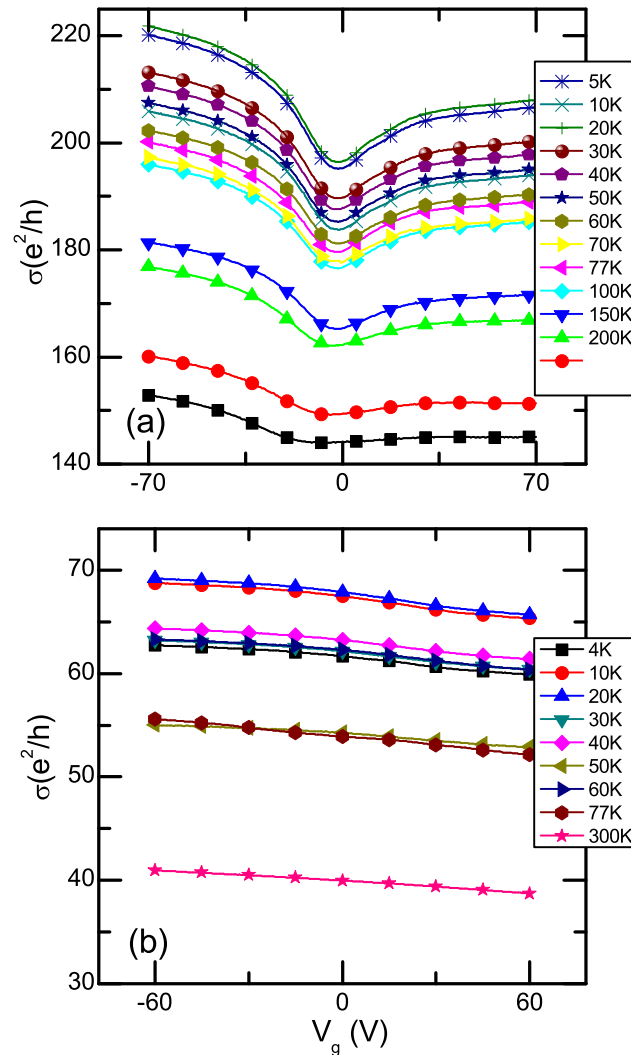
Figure 3.5 : DC transport data from (a) gold (L=20 nm, $\mu_{20K} = 4.8 \times 10^2$ cm^2/V·s) and (b) platinum (L=50 nm, $\mu_{20K} = 3 \times 10^1$ cm^2/V·s) short channel devices. The voltage across the source-drain electrodes was fixed at 100mV. For the gold devices in (a) a clear CNP evolves as $T \rightarrow 0K$ whereas the devices in (b) have a CNP shifted to $+V_G$. The gate voltages are different between devices (a) and (b) because of oxide defects in device (b). This was causing shorts to the substrate. Adapted from reference [7].

charge density. The effects seen in the figure are unlikely to be from contamination, however, because both gold and platinum devices were handled in identical manners, and any contamination present in one device should be present in the other. If contamination were present, both gold and platinum devices should show shifts in their CNP. Further, because of the small active region of the transistor, the likelihood of contamination being present in that particular area is reduced. Nevertheless, should any contamination be present, devices were annealed in vacuum for 16h at 100°C and were then measured.

Because of contamination during the fabrication process, it is difficult to know the true work function of our metal contacts as it can cause shifts in the metal work function due to intrinsic dipole moments of surface adsorbates[34], which makes predicting the doping near the contacts difficult. However, since both platinum and gold electrodes were handled in similar ways, it is likely that the same adsorbates are on each metal contact leading to similar shifts in work function. Previous scanning potentiometry experiments[37] have shown that platinum maintains a higher work function than gold, even after being exposed to ambient conditions.

As shown in figure 3.5, devices made with platinum contacts present a large shift in the CNP whereas devices made with gold contacts do not. We observed this trend (down to cryogenic temperatures) on 8 additional platinum devices and 9 additional gold devices. Because of the differences in chemical potential between graphene and the gold and platinum contacts, the local charge density will change as charges flow to equalize the imbalance. The direction of electron flow (into or out of graphene) will ultimately be determined by where the equilibrated chemical potential lies within graphene's band structure - electron accumulation if it lies above the Dirac point or electron depletion if it lies below the Dirac point.

The data shown in figure 3.5 are consistent with electron depletion (hole accumulation) in the case of platinum contacts, based on the shift in CNP and broadening of the $I_{DS} - V_G$ curves[57, 104]. The gold electrodes appear to do little to change
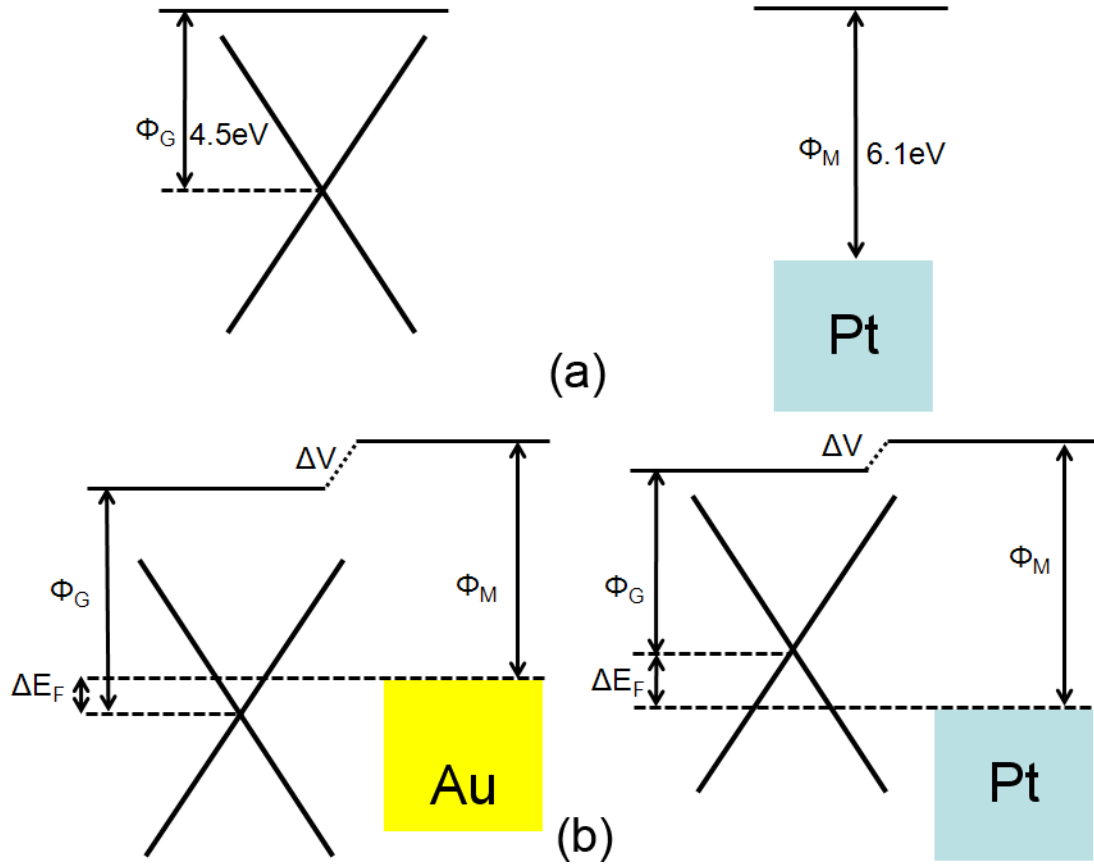
Figure 3.6 : (a) Schematic of the vacuum-level alignment before contact is made between graphene and a metal (Pt in this case) and (b) band-gap alignment at the metal-graphene interface once contact is made. Based on the work in reference [8], it is possible that gold electrodes will not $p-$type dope graphene, and could possibly be a weak $n-$type donor.

the local charge environment in graphene, as the CNP stays near 0 V_G. As the work function of graphene lies at 4.5eV and the work functions of gold and platinum are typically reported to be 5.4eV and 6.1eV (in vacuum), how is it that gold is not also a hole donor for graphene? As mentioned above, metal work functions can be altered such that the values measured in vacuum are significantly different than those measured in an experimental system. Additionally, theoretical calculations have shown[8] that the work function required for metal contacts to transfer holes into graphene may be greater than 5.4eV. This is illustrated in figure 3.6. In figure 3.6(a), both the

metal and graphene are separated and not in contact, so both exhibit vacuum-level alignment. However, as the metal and graphene are brought into contact, the wave functions of both materials begin to overlap and a shift in the position of the chemical potential occurs as charges move across the metal-graphene interface. This establishes a built-in potential, $\triangle V$ because of the local interface dipole present. If gold establishes a larger built-in potential, it could shift the chemical potential above the Dirac point, making gold a weak $n-$type donor. If some contamination was present on the gold electrodes to slightly lower its work function, this would be consistent with the results we see in figure 3.5(a). Note that this value reported in reference [8] is strongly dependent on the separation distance between graphene and the contact, suggesting that our samples may have very little separation between the electrodes and graphene directly at the nanogap.

In order to obtain a quantitative measure of the amount of doping in the channel, the gate can be used to recover the CNP and therefore the dopant density using $n = C_G V_G / e$ where $e = 1.6021 \times 10^{-19}$C. For gold electrodes, the largest gate voltage required to reach the CNP was $V_G = -7$V, corresponding to a charge density of 3.2×10^{12} cm^{-2} electrons. For the platinum electrodes, the CNP could not be reached experimentally, so the lower bound on charge density in the channel is $n = 2.72 \times 10^{13}$ cm^{-2} holes.

Once the devices were measured, more aggressive annealing was used only for the platinum electrodes. The 400°C temperatures used in the annealing process cause the gold nanogap devices to develop electrical shorts. After the high temperature annealing outlined in section 3.2.2 was complete, the platinum electrodes were tested again with minimal change in device behavior as compared to figure 3.5. Five platinum devices out of twenty-seven showed a measurable CNP after annealing, with the one closest to $V_G = 0$ occurring at $V_G = 38$V, which gives $n = 1.73 \times 10^{13}$ cm^{-2} holes for that device. The remaining twenty-two platinum devices annealed do not show a change in CNP. These data strongly suggest that platinum (with possible

work function modifying adsorbates) is a significant donor of holes into graphene, increasing the charge carrier density by an order of magnitude over gold-based devices. Similar results to those presented in this section have been created using top contact graphene transistors[105], but the graphene was placed directly on the SiO_2 substrate. The influence of the oxide on the graphene must be taken into account and makes the analysis in this case murky. In addition, the authors used a thin ($<$1 nm) layer of chromium as an adhesion layer for gold. This presents a Au/Cr interface to the graphene, making work function determinations even more difficult than presented in this section.

3.3.2   Interdigitated Electrodes with $L \geq 1\mu$m

To verify the above experimental evidence and to establish an upper bound on charge transfer, we measured the interdigitated electrodes present on the chip. The data from the transmission-line measurements is shown in figure 3.7. The lack of significant shift in CNP in these devices is directly related to the longer channel lengths. As L increases, the overall influence of the contacts on graphene within the channel decreases. Eventually, once a minimum channel length distance is exceeded, the charge density within the graphene furthest from the contacts will return to the bulk value. Consequently, as compared to the short channel devices presented previously, long channel gold- and platinum-based electrode devices should show no shift in CNP.

Immediately after fabrication, however, these devices both showed a shift in CNP to $+V_G$. Annealing at 100°C for 16h in vacuum showed no change, so the devices were annealed at 400°C for 1h in Ar/H_2, then annealed again at 100°C for 16h in vacuum. The data shown in figure 3.7 are from this final annealing step. They each share a similar shift in CNP, possibly due to additional adsorbates not removed during the annealing process or interactions with the oxide[82]. Comparing the data in figure 3.7 to that in figure 3.5 suggests that the maximum distance for charge diffusion from the contacts is $<$ 500 nm (half the length of the smallest device with this
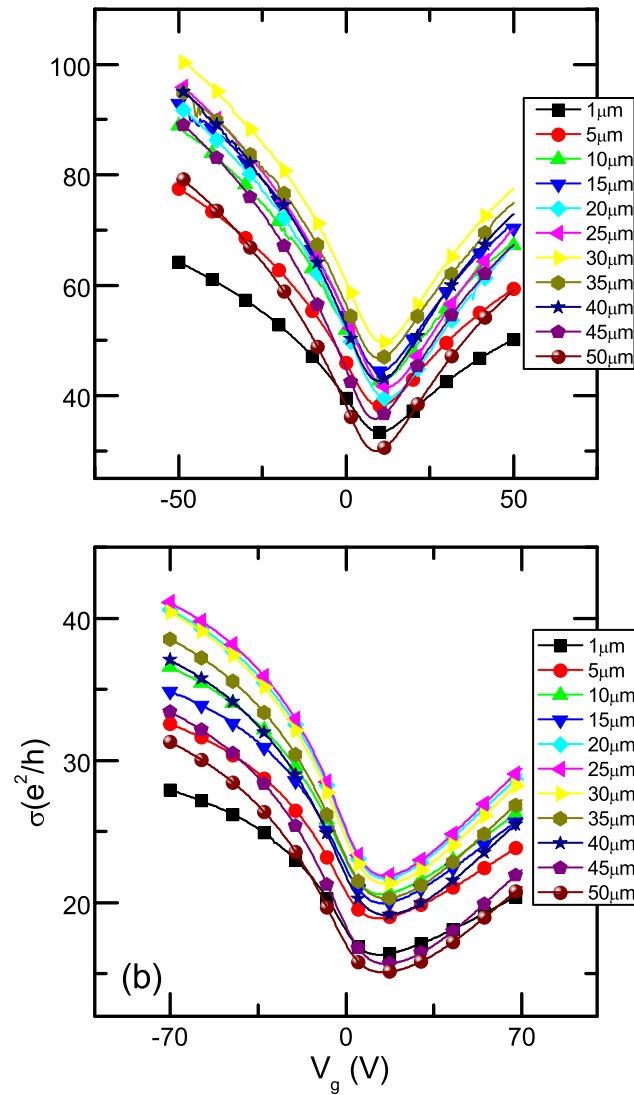
Figure 3.7 : DC transport data from (a) gold ($\mu_{300K} = 3.0 \times 10^3$ cm²/V·s) and (b) platinum ($\mu = 1.0 \times 10^3$ cm²/V·s) electrodes. Channel lengths range from 1μm - 50μm. Gate voltage differences between gold and platinum reflect oxide weakness in (a), but this does not alter the analysis. The source-drain bias was fixed at 100mV and devices were measured at 300K. A slight difference in neutrality point may be present due to the differing x-axes above, but the difference is small compared to figure 3.5. Adapted from reference [7].

geometry), consistent with previously reported results[92, 88]. The higher measured mobility in these samples as compared to the nanogap devices may be due to better gate coupling between the graphene and the substrate or the longer channel length devices have sufficient room for wrinkles and folds to flatten out before reaching the second electrode.

3.4   Conclusions

In this chapter, data on suspended graphene transistors with sub-50 nm channel lengths has been presented. For platinum electrodes, large shifts in the CNP are observed even after significant thermal annealing to remove contamination from the fabrication process. The gold electrodes studied do not show this shift in CNP. This strongly suggests that platinum electrodes modify the charge density near the metal/graphene interface by donating holes to the graphene. This may be due to a shift in the chemical potential in graphene as the wave functions between graphene and contacts begin to overlap. However, as the channel length increases, the disparity between gold and platinum electrodes disappears, allowing the conclusion that the upper limit of charge transfer in this CVD-grown graphene is less than 500 nm.

The fabrication process presented here allows for the creation of suspended graphene transistors with minimal processing and alignment. The nanogaps are self-aligning, in that the resultant gap between the final electrodes will be parallel with the first electrode deposited. The deposition of CVD graphene onto these electrodes is repeatable and fairly easy to perform, opening the door to additional suspended graphene transistor geometries. By isolating the graphene from the substrate using this simple method, the possibility to create high mobility electronics and efficient photovoltaic devices becomes easier and more scalable.

Chapter 4

Gigahertz Probing of Poly-3(hexylthiophene) with a Kilohertz Detection Scheme

4.1   Introduction

This chapter will focus on an ongoing research project involving microwave probing of poly-3(hexylthiophene) (P3HT). Charge carrier dynamics in organic films have been well-studied at DC using field-effect mobility measurements [65, 16, 17, 106, 21]. Charge transport within these materials has been described by activated hopping transport[66] with emphasis on the primary injection event of charge carriers from the metal contact into the organic semiconductor[107]. The DC transport behavior of organic semiconductors from 300K to 4K is also covered in chapter 2. While DC transport studies are crucial for elucidating charge carrier dynamics, little is known about the nature of transport for the fastest charge carriers.

Performing time-of-flight (TOF) measurements on organic semiconductors gives information about the drift mobility, which is directly related to the distribution of charge traps within the material as well as charge injection dynamics[108, 109]. In TOF measurements, charge carriers are generated by the application of a fast (ns or shorter) optical or electrical pulse at one electrode, and the time required for carriers to migrate to the opposite electrode is recorded. As charges encounter traps, their velocity slows or they become energetically bound to the trap, causing measurable changes in the mobility. Terahertz study of acene derivative organics has shown band-like transport mediated by electron-phonon interactions [110]and the nature of traps within these materials[31].

Equally important to transient charge carrier dynamics is the behavior of charge

carriers when in the presence of an alternating voltage source. The characteristics and properties of organic semiconductors when operated in the MHz and GHz regimes is of great technological importance in radio-frequency identification (RFID) [111, 112, 113] chips, high-frequency rectifiers [114, 115], high-frequency electronics [116], and field-effect transistors operating at kHz frequencies and above[117]. A recent study of P3HT from DC to 12GHz has revealed the influence of the hexyl side groups on the dielectric relaxation and reduction in hopping activation energy at frequencies greater than a few kHz[118]. An additional study on holes in poly(p-phenylene vinylene) found that the space charge present in PPV caused an inductive contribution to the AC admittance, causing a lag in the AC response due to charge dispersion [119]. However, little work has been done to investigate the high-frequency behavior of mobility in organic semiconductors.

To address this, a method is proposed for measuring mobilities in the MHz and GHz range. This method utilizes two microwave sources with one slightly detuned from the other. By using the transistor as a non-linear mixer, the two high-frequencies are mixed, and a sum and difference frequency are generated. The difference frequency is measured with a lock-in, thereby capturing the high-frequency behavior without the need for high-speed microwave detectors. This method is still under development and analysis, with this chapter serving to outline the basic method, experimental setup, and current data.

4.2   Motivation and Theoretical Background

The impetus for the method presented in this chapter stems from the use of alternating current scanning-tunneling microscopy[120] (ACSTM). In a previous work[38], ACSTM was used in order to probe charge density variation versus contact metal work function in P3HT. Due to variations in charge density under the STM tip, changes in capacitance will occur which will be detected as a $\partial C/\partial V$ signal. Two microwave signals are applied, separated by a difference frequency $\Delta\omega = \omega_1 - \omega_2$,

where $\Delta\omega = 4$kHz. The STM junction can be modeled as a non-linear lumped R-C (resistor-capacitor) element, with the non-linearity enabling the mixing of the two RF signals. Performing a Taylor expansion of the measured capacitive signal about the bias voltage (V_0), one obtains

$$I_t = \cdots + \frac{1}{2} \left.\frac{\partial C}{\partial V}\right|_{V_0} (\Delta\omega) V^2 \sin\left((\Delta\omega)\, t\right) + \cdots \tag{4.1}$$

which gives the $\partial C/\partial V$ signal measured at the difference frequency of the two microwave input sources. Based on the success of this technique, the replacement of the STM tip with an organic field-effect transistor (FET) device was natural. FETs have two regions where mixing can occur, shown in figure 4.1.

The mathematical analysis of the organic FET is similar to the ACSTM case above. However, instead of only obtaining the $\partial C/\partial V$ signal, one also obtains a signal proportional to $\partial^2 I/\partial V^2$. This $\partial^2 I/\partial V^2$ term is related to the conductivity of the P3HT, but measured at microwave frequencies. By performing a similar Taylor expansion of the measured signal, one obtains

$$\begin{aligned}
I = \cdots &+ \frac{1}{2} \left.\frac{\partial^2 I}{\partial V^2}\right|_{V_0} \left(V \cos\left(\omega_1 t\right) + V \cos\left(\omega_2 t\right)\right)^2 + \cdots \\
\cdots &+ \left.\frac{\partial C}{\partial V}\right|_{V_0} \left(V \cos\left(\omega_1 t\right) + V \cos\left(\omega_2 t\right)\right)\left(-\omega_1 V \sin\left(\omega_1 t\right) - \omega_2 V \sin\left(\omega_2 t\right)\right) + \cdots .
\end{aligned}$$
$$\tag{4.2}$$

Focusing first on the $\partial^2 I/\partial V^2$ component and performing the relevant algebra,

$$\frac{1}{2} \left.\frac{\partial^2 I}{\partial V^2}\right|_{V_0} V^2 \left(1 + \frac{1}{2}\cos\left(2\omega_1 t\right) + \frac{1}{2}\cos\left(2\omega_2 t\right) + \cos\left(\left(\omega_1 + \omega_2\right) t\right) + \cos\left(\left(\omega_1 - \omega_2\right) t\right)\right),$$
$$\tag{4.3}$$

and focusing on the difference frequency piece, the detected signal at the difference

frequency becomes

$$I_{diff,resistive} = \frac{1}{2} \left. \frac{\partial^2 I}{\partial V^2} \right|_{V_0} V^2 \cos\left(\left(\omega_1 - \omega_2\right)t\right). \qquad (4.4)$$

A similar procedure is performed for the $\partial C/\partial V$ component in equation 4.2, and after focusing on the difference frequency piece, one obtains

$$I_{diff,capacitive} = -\frac{1}{2} \left. \frac{\partial C}{\partial V} \right|_{V_0} V^2 \left(\omega_1 - \omega_2\right) \sin\left(\left(\omega_1 - \omega_2\right)t\right). \qquad (4.5)$$

By performing a double integration on equation 4.4 and a single integration on equation 4.5, one could expect to obtain $I - V$ and $C - V$ data from the FET correlated to the GHz response of the charge carriers, respectively.

In the organic FET, non-linearities in the transistor provide the RF mixing. There are multiple possible sources of non-linearities in these devices, including the contact interfaces between the organic semiconductor and the metal electrodes, and the response of the channel region itself. The most common non-linearity encountered is a Schottky barrier, but *any* non-linearity at the interface between the contact and the organic semiconductor will lead to mixing. If the value of the metal work function is smaller than the polaron formation energy in the semiconductor, vacuum alignment occurs between the metal and semiconductor and a Schottky barrier is formed[47, 46]. See section 1.1.3 for a more complete explanation. A Schottky barrier has a non-linear response, $I \propto \exp\left(\frac{\phi_B}{V_T}\right) \exp\left(\frac{V_D}{V_T}\right)$, where ϕ_B is the barrier height, V_D is the voltage across the Schottky contact, and $V_T = k_B T$. With the Schottky barrier, the two microwave signals will be mixed. This will create a mixed AC signal that will be superimposed on any DC bias applied to the FET. Using the lock-in to detect this will then result in the detection of a DC signal with an AC perturbation on top, yielding the DC bias once the signal from the lock-in is integrated. A Schottky contact often manifests itself as a non-linear DC $I_D - V_D$ response at low V_D.[121]

The second source of non-linearity in a FET lies in the crossover region between the
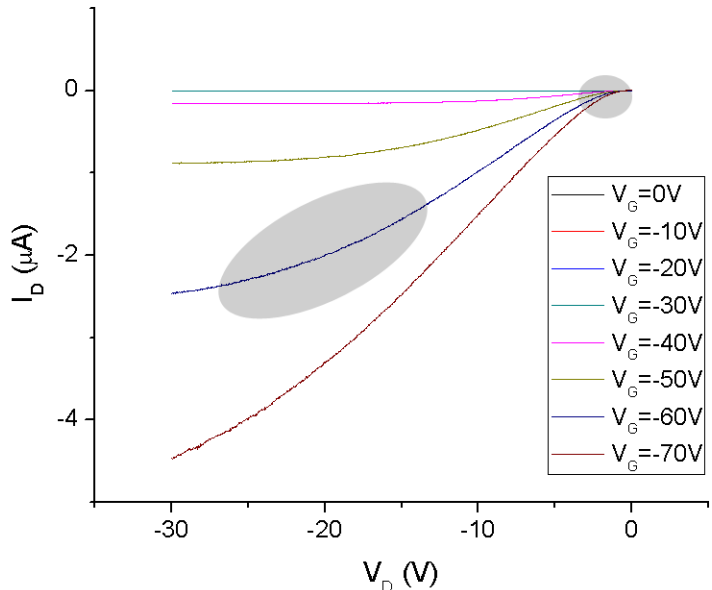
Figure 4.1 : A representative I_D-V_D plot for various gate voltages for a 5μm channel length device using gold electrodes. The regions highlighted in gray are areas of nonlinear DC transport where RF mixing can occur. The region on the right is likely due to a non-linearity at the contact whereas the region on the left is due to the FET entering the saturation regime.

linear regime and saturation regime of the DC I_D-V_D curve. Should the mixing occur *within* the transistor as opposed to at the contact, the signal measured by the lock-in should have some relationship to intrinsic properties of the organic semiconductor. It is this signal that would be twice integrated in order to obtain $I-V$ data from AC transport. Figure 4.1 shows the two regions where mixing can occur in an organic FET.

4.3   Sample Fabrication and Experimental Setup

The electrode geometry for this experiment is fairly simple when compared to previous chapters. The standard interdigitated transmission line electrodes were lithographically defined using the SEM and 1 nm of titanium followed by 15 nm of gold or platinum was deposited using electron beam deposition. We also fabricated chromium

and copper electrodes to to intentionally produce energetic misalignment between P3HT and the electrodes. A device with alternating gold and platinum electrodes was also fabricated. Electrodes were cleaned in oxygen plasma for two minutes prior to depositing the P3HT. The organic layer was deposited using the spincoater set to 750 RPM. The substrate was allowed to begin spinning and then a drop of P3HT as added slightly off-center from the electrodes. Once the film over the electrodes was verified to look clean in an optical microscope, a gate contact was created by etching through the oxide with a diamond scribe and adding an indium point contact. The entire substrate was then placed into the vacuum probe station where it was pumped on at 100°C for 16h.

The experimental setup is shown in figure 4.2. Two microwave sources are used, where one is detuned from the other by a small amount (in this case, $\Delta f = 4$kHz). They are combined into one signal where a small part of the total power is diverted to the lock-in amplifier to serve as the reference signal. The remaining signal is injected into the FET through a bias-tee along with a DC voltage that biases the transistor through the linear regime and into the saturation regime. The RF signal mixes somewhere within the transistor, possibly including its contacts, and generates the sum and difference frequencies shown in equation 4.3. The low-frequency mixed signal is extracted using a second bias-tee (with the RF port terminated using a 50 Ω terminator), passed through a current amplifier set to high-pass filter mode, and detected by the lock-in. Care was made to ensure that no mixing occurred in the cabling or probe station, meaning the two microwave signals should be unperturbed up until their interaction with the FET.

The probe station was outfitted with high-frequency rigid coaxial cabling that enabled a direct connection of the SMA cables used in the microwave frequency generation equipment to be connected to the probe tips. The upper limit on frequency supported in the probe station is 1GHz; therefore, all input frequencies are at this value and lower. No attempt at impedance matching was attempted, mostly because
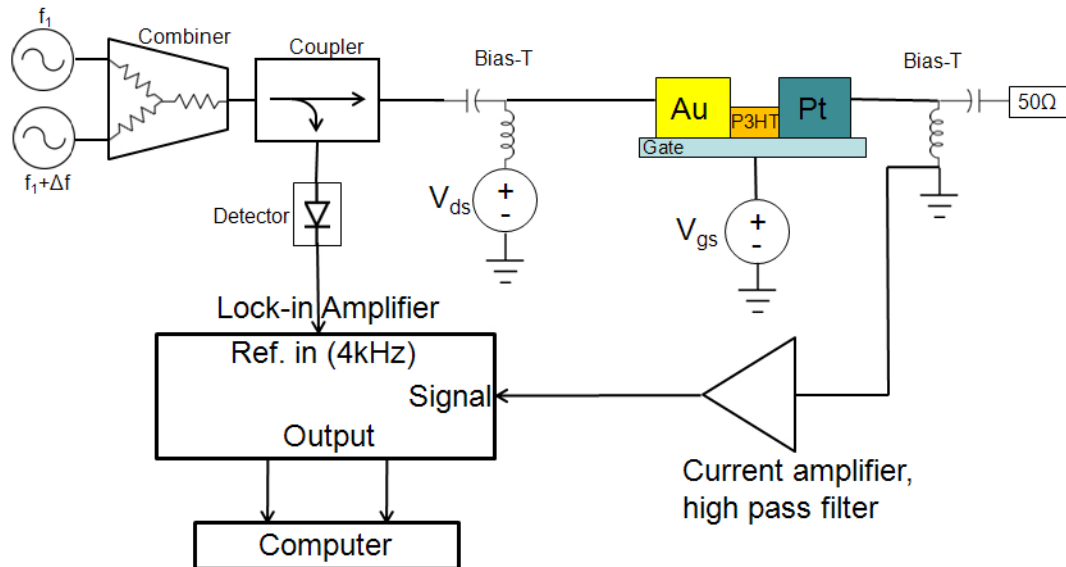
Figure 4.2 : Experimental setup for RF probing of P3HT. Two microwave sources are used, one at $f_1 = 100 - 1000$MHz and $f_2 = f_1 + \Delta f$ where $\Delta f = 4$kHz. The amplitudes of the RF signals are set to 10dBm. The signals are combined into one, where 10% of the power is diverted to the detector which is fed to the lock-in as the 4kHz reference signal. The remaining RF signal is sent through a bias-tee and, coupled with a DC bias, into the device. Mixing occurs within the transistor, and then the mixed (low-frequency) signal is extracted using a second bias-tee. The RF part of this second bias-tee is 50Ω terminated. The low-frequency signal passes through a current amplifier which acts as a high-pass filter (to remove the DC component of the signal) and is then detected by the lock-in. The data is then fed to a computer. A second configuration swaps the RF connections on the bias-tees. This has RF injection on the "ground" side of the transistor and the RF termination on the DC-bias side. In this figure, the hybrid Au/Pt device is shown. Other configurations used a single metal for all contacts.

the P3HT device has an unknown AC impedance and a DC response that depends strongly on biasing conditions. To combat this problem, the input power was increased until a measurable signal was obtained by the lock-in.

The measurement procedure was designed to bias the FET through the linear regime and into the saturation regime. Because of the nature of organic FETs, large source-drain voltages were required in order to bias the FET into saturation, often in excess of 30 V_{DS} at the largest gate voltage values. The frequency response as a function of channel length was recorded, as was gate dependent data at various input frequencies. Additionally, frequency dependent data were collected where the frequency was swept from 100MHz to 1GHz with a fixed channel length.

4.4 Experimental Results and Discussion

Data presented here were obtained from the Au/Pt hybrid device, which exhibited the highest measured conductivities and had very linear response at low source-drain bias. This suggests that the contacts should be ohmic in nature, thus reducing the possibility of mixing due to a Schottky barrier. Based on the transmission line analysis, the mobility of the P3HT is 0.06 cm^2/V·s at $V_G = -70$V and the dominant resistance in the device comes from the channel. Based on experimental[122] and theoretical[107] results, the charge injecting contact most strongly controls device behavior. Therefore, the recorded data should reflect the interaction between P3HT and the injecting contact. By designing our testbed with alternating Au and Pt electrodes, our transistor maintains a constant film morphology within the channel and removes concerns about the influence of film morphology on frequency response.

4.4.1 Frequency response for a fixed channel length

First, the frequency response of P3HT will be presented for two different channel lengths, 1 μm and 10 μm, for Au and Pt injecting contacts. Both in-phase and out-of-phase data will be presented. Similarities between the in-phase and out-of-phase

data suggests there is a phase offset between the reference signal and the detected signal. The origin of this phase offset is likely due to a capacitive phase shift from the organic FET.

Figure 4.3 shows the in-phase and out-of-phase frequency response for a 1 μm channel length Au-injection and Pt-injection device. Figure 4.4 shows data for a 10 μm channel length device. Clear differences between frequency response, injecting electrode, and channel length are visible.

For the 1 μm Au-injection data, 400MHz appears to be the preferred AC frequency, with the frequency response decreasing in current as the driving frequency increases. The reason for this peak at 400MHz is unclear. The data for the 1 μm Pt-injecting contact is more monotonic with the frequency response decreasing in current as the driving frequency increases. One possible explanation for this behavior is that as the AC frequency increases, fewer charge carriers have time to cross the channel before they are driven in the opposite direction. At higher frequencies, the charge carriers may become more localized, leading to a reduction in conductivity. Note that as frequency increases, the entire measurement apparatus becomes more lossy, which could also explain the decrease in the measured lock-in signal with increasing frequency. As the source-drain bias is increased, an increase in conductivity is also noted across all frequencies. Simulations performed in reference [109] suggest that the carrier transit time decreases with increasing source-drain bias. Consequently, as the source-drain bias is increased, it is possible that more charge carriers can traverse the channel during the half-wave period of the AC signal, thereby increasing the conductivity.

The 10 μm data in figure 4.4 are harder to interpret. There is no reason to expect a peak in conductivity until the highest source-drain bias is reached, based on simulations in reference [109]. Part of the shape of these curves lies in the possibility of mixing occurring at the contact as opposed to within the transistor channel. Later in this chapter, frequency response curves will be singly integrated to show their
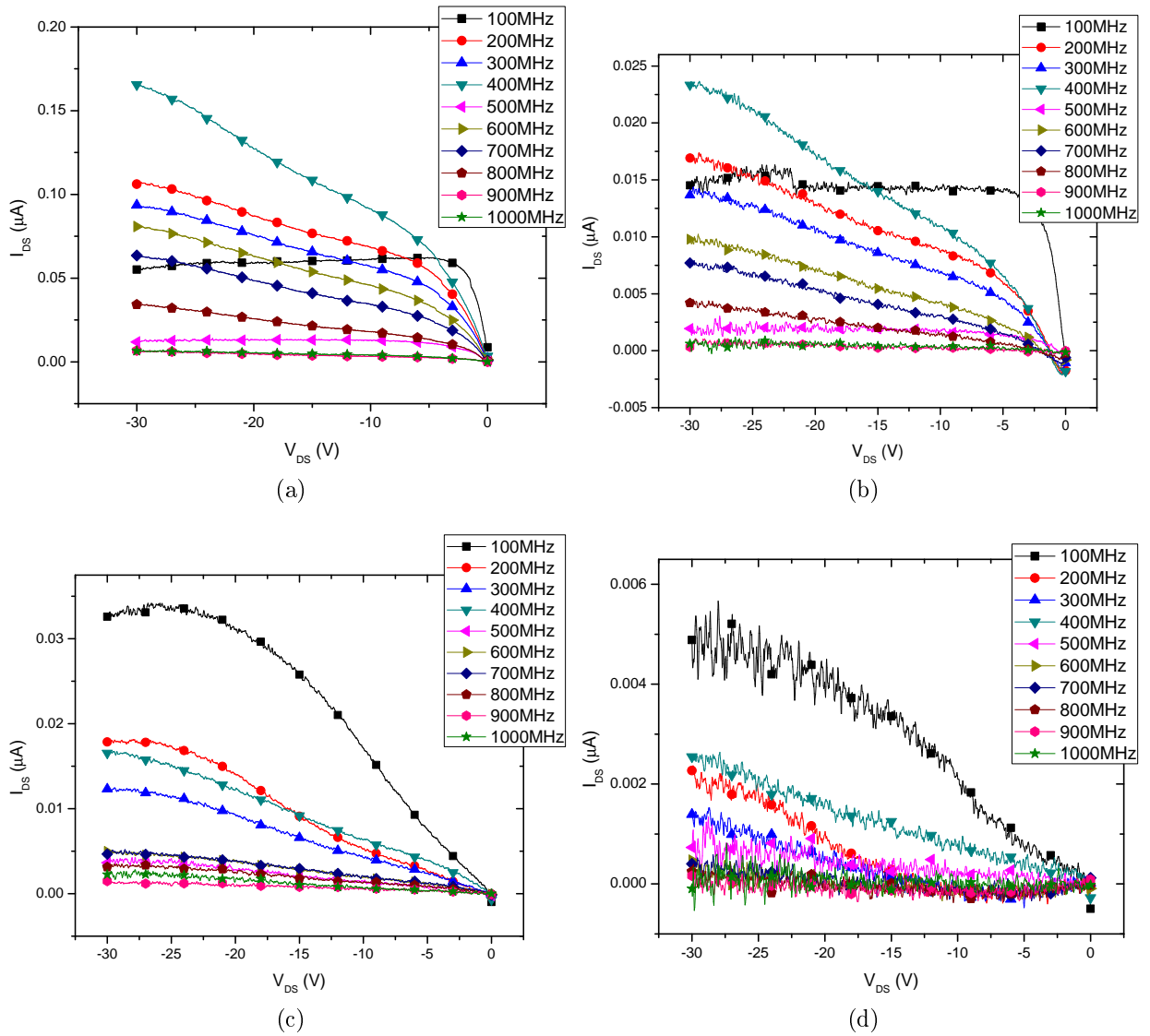
Figure 4.3 : Frequency response for 1 μm channel length Au- ((a), in-phase, and (b), out-of-phase) and Pt-injection ((c), in-phase, and (d), out-of-phase) devices. Note the dissimilar response when injecting from the Au or Pt contact.

Figure 4.4 : Frequency response for 10 μm channel length Au- ((a), in-phase, and (b), out-of-phase) and Pt-injection ((c), in-phase, and (d), out-of-phase) devices. Note the dissimilar response when injecting from the Au or Pt contact, as well as differences from figure 4.3.

correspondence to measured DC $I - V$ curves. The shapes of those curves are similar to the ones shown in figure 4.4.

4.4.2 Effect of gate voltage on measured signal at lock-in

Next, the effect of gate voltage on measured signal will be presented for 1 μm and 10 μm channel length devices. Figure 4.5 shows the in-phase and out-of-phase response for a 1 μm device at a fixed driving frequency of 100MHz. Figure 4.6 shows data for the 10 μm device. Interpretation of these results is equally difficult. It is clear, however, that increasing the gate voltage increases the response recorded by the lock-in. Whether this behavior is due to the intrinsic properties of the polymer, a reduction of the injection barrier energy level, or is instead related to the DC transport, is difficult to ascertain.

4.4.3 Integration of the mixed-signal response

As mentioned in section 4.2, integrating the in-phase and out-of-phase response might yield information about the high-frequency behavior of charge carriers. For our data, however, a single integration of the mixed-signal microwave data gives curves that look similar to DC transport curves. Doing a second integration gives curves that do not seem to have any obvious relationship to $I - V$ transport curves. Figures 4.7 and 4.8 contain the singly integrated curves for injection with the Au contact at 100MHz and 1GHz, and figures 4.9 and 4.10 contain the curves for injection with the Pt contact for 100MHz and 1GHz. The dotted lines in the figures are the integrated curves and the solid lines are the measured DC curves.

As channel length increases, the correspondence between the integrated curves and DC transport curves improves. At short channel lengths, however, there is an increased discrepancy. This would suggest that for longer channel devices, mixing of the microwave signal is occurring at the contact and is then superimposed on the DC bias signal; this is occurring even though Pt should make Ohmic contact to
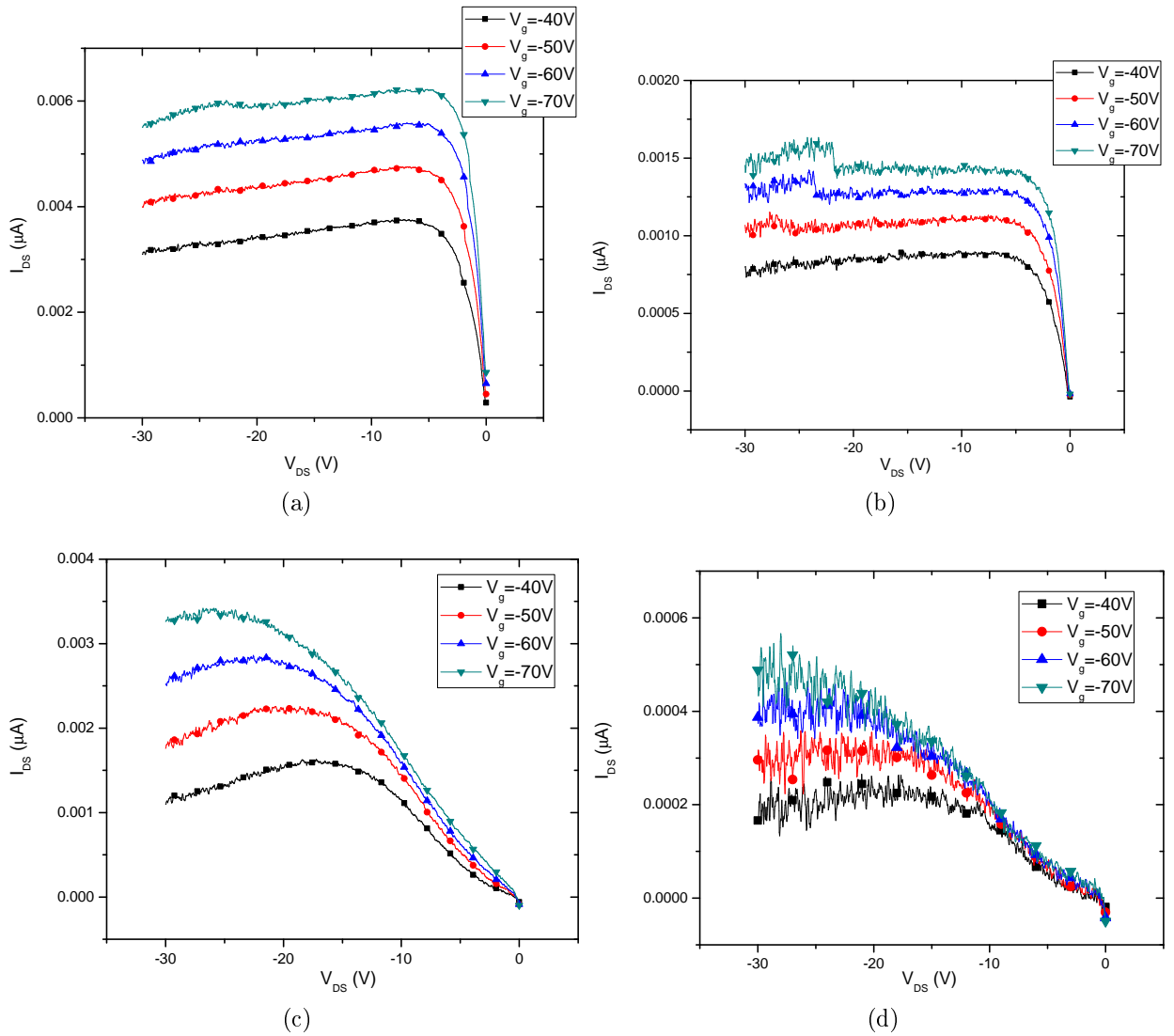
Figure 4.5 : Gating effect on conductivity for 1 μm channel length Au- ((a), in-phase, and (b), out-of-phase) and Pt-injection ((c), in-phase, and (d), out-of-phase) devices at a fixed frequency of 100MHz. Note the dissimilar response when injecting from the Au or Pt contact.

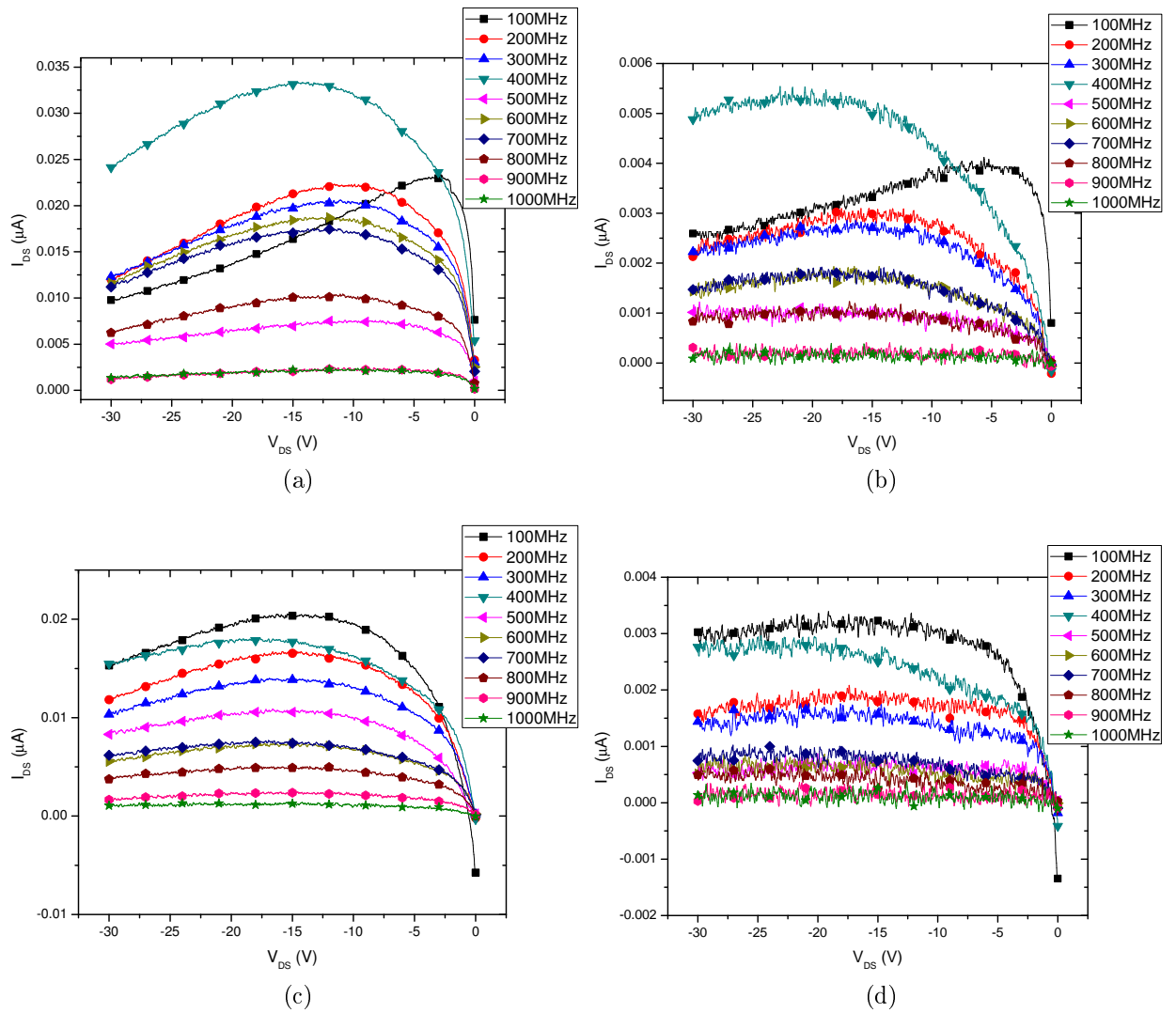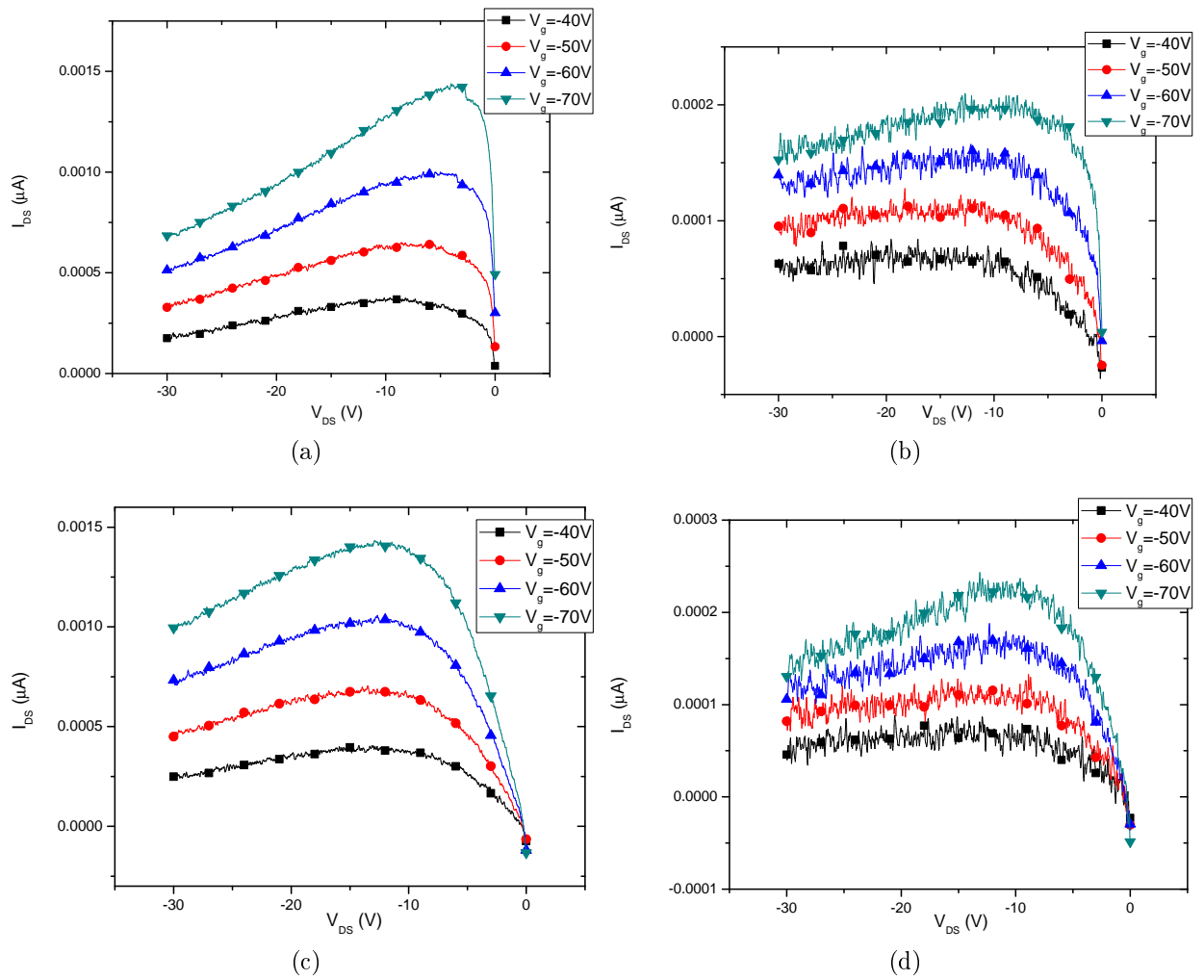Figure 4.6 : Gating effect on conductivity for 10 μm channel length Au- ((a), in-phase, and (b), out-of-phase) and Pt-injection ((c), in-phase, and (d), out-of-phase) devices at a fixed frequency of 100MHz. Note the dissimilar response when injecting from the Au or Pt contact.
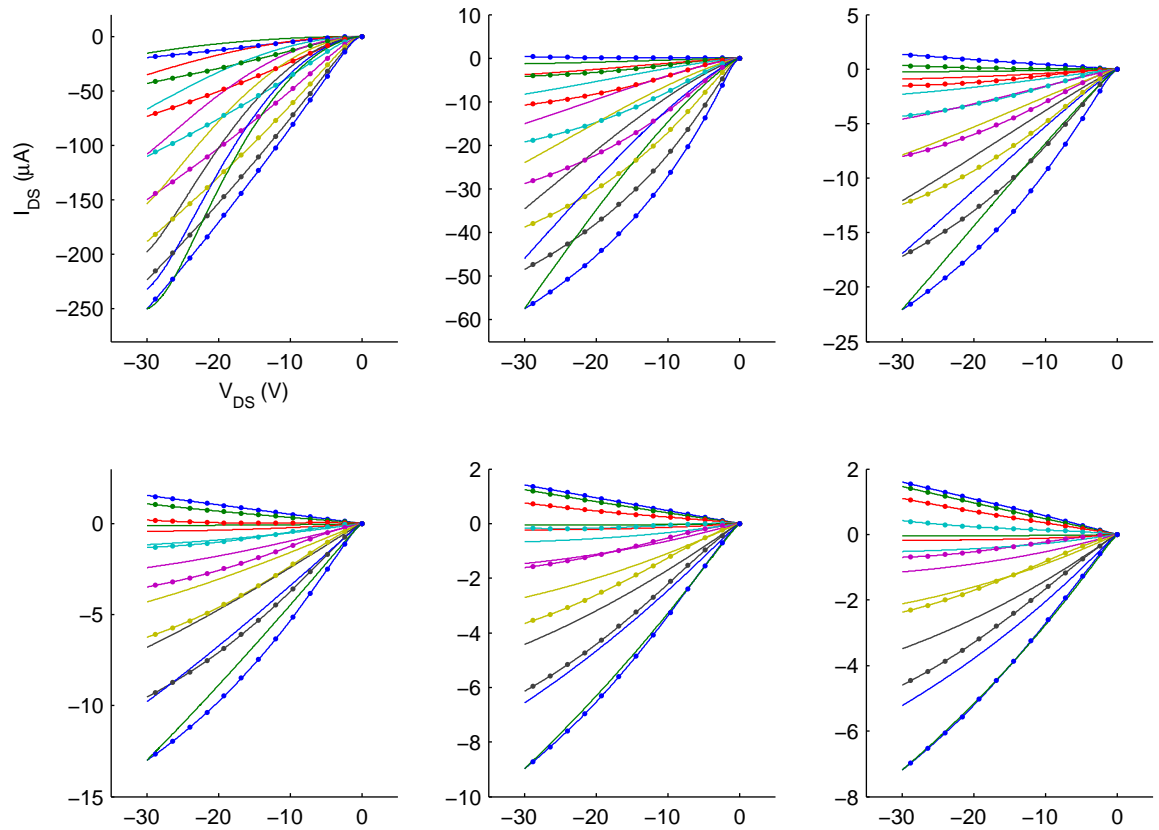
Figure 4.7 : Au-injection at 100MHz. Dotted lines are integrated curves, smooth lines are the measured DC $I-V$ curves. The integrated curves are scaled to the maximum value in the DC curves, using a single scaling value. Top, from left to right: 1 μm, 5 μm, 10 μm. Bottom, from left to right: 15 μm, 20 μm, 25 μm. Gate voltage range in each plot is from 0V (top curve) to -70V (bottom curve).
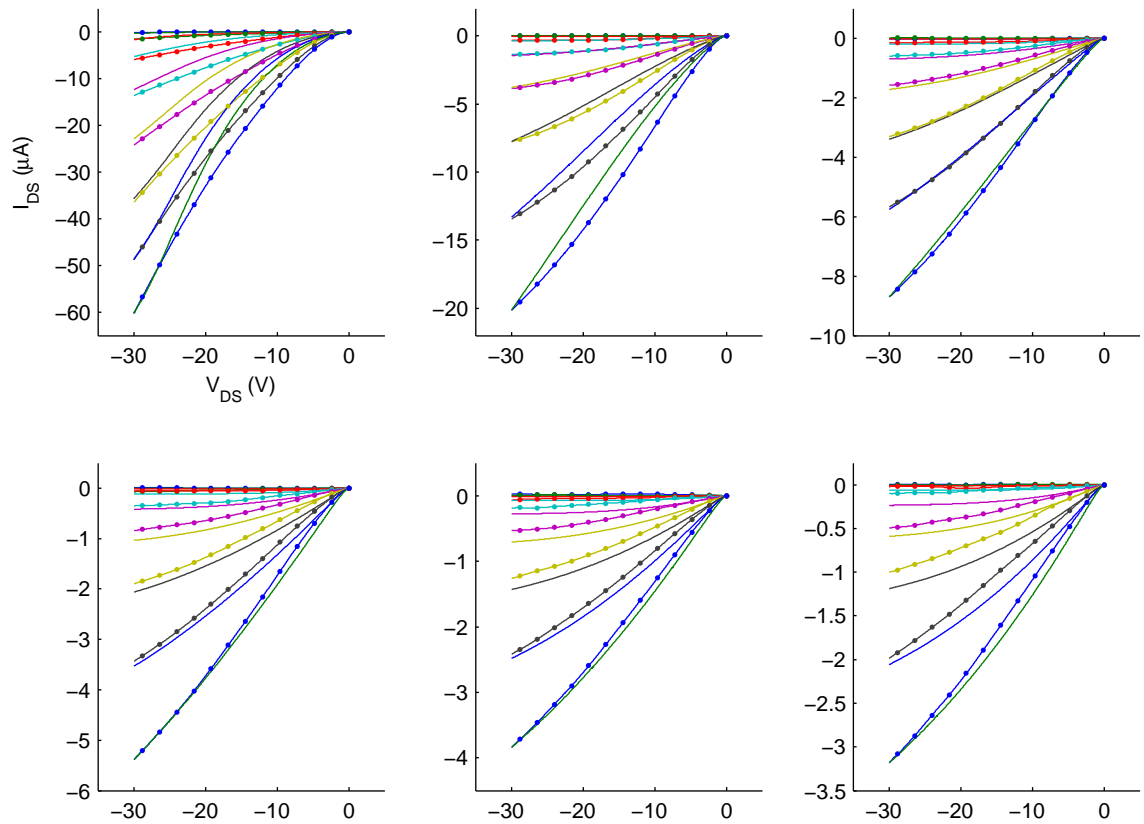
Figure 4.8 : Au-injection at 1GHz. Dotted lines are integrated curves, smooth lines are the measured DC $I-V$ curves. The integrated curves are scaled to the maximum value in the DC curves, using a single scaling value. Top, from left to right: 1 μm, 5 μm, 10 μm. Bottom, from left to right: 15 μm, 20 μm, 25 μm. Gate voltage range in each plot is from 0V (top curve) to -70V (bottom curve).
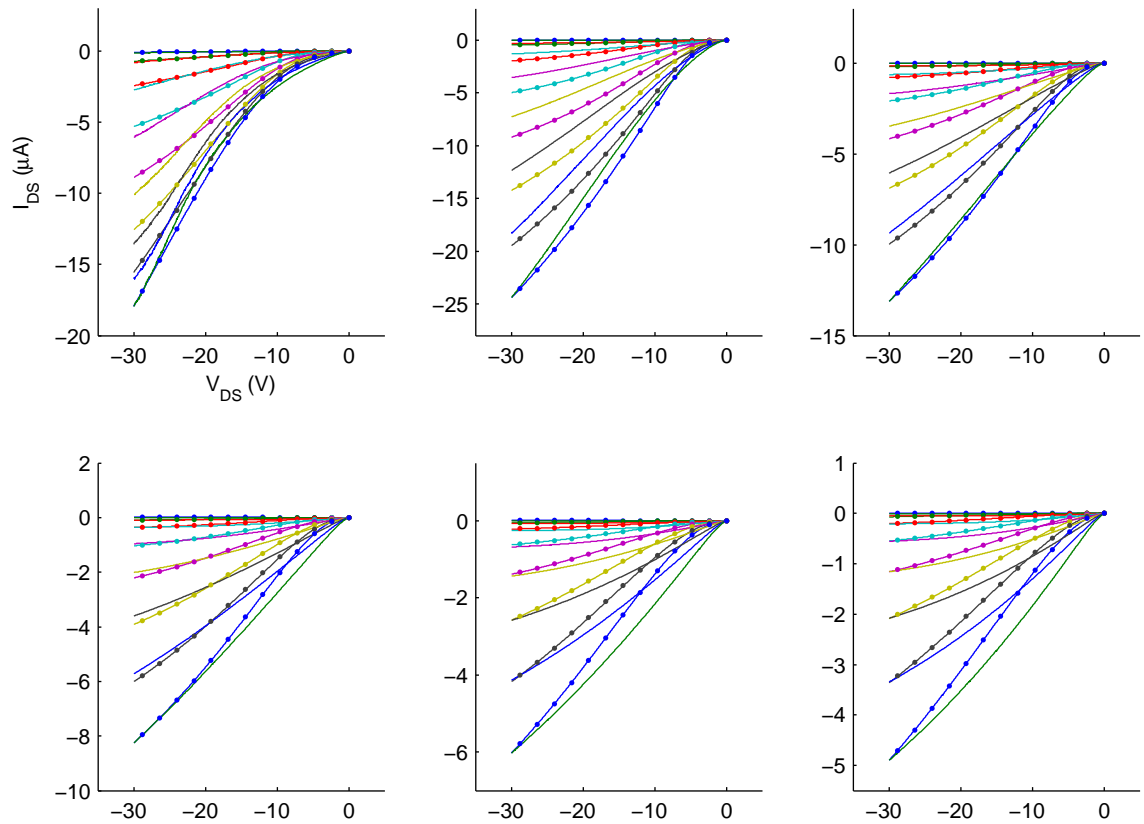
Figure 4.9 : Pt-injection at 100MHz. Dotted lines are integrated curves, smooth lines are the measured DC $I-V$ curves. The integrated curves are scaled to the maximum value in the DC curves, using a single scaling value. Top, from left to right: 1 μm, 5 μm, 10 μm. Bottom, from left to right: 15 μm, 20 μm, 25 μm. Gate voltage range in each plot is from 0V (top curve) to -70V (bottom curve).
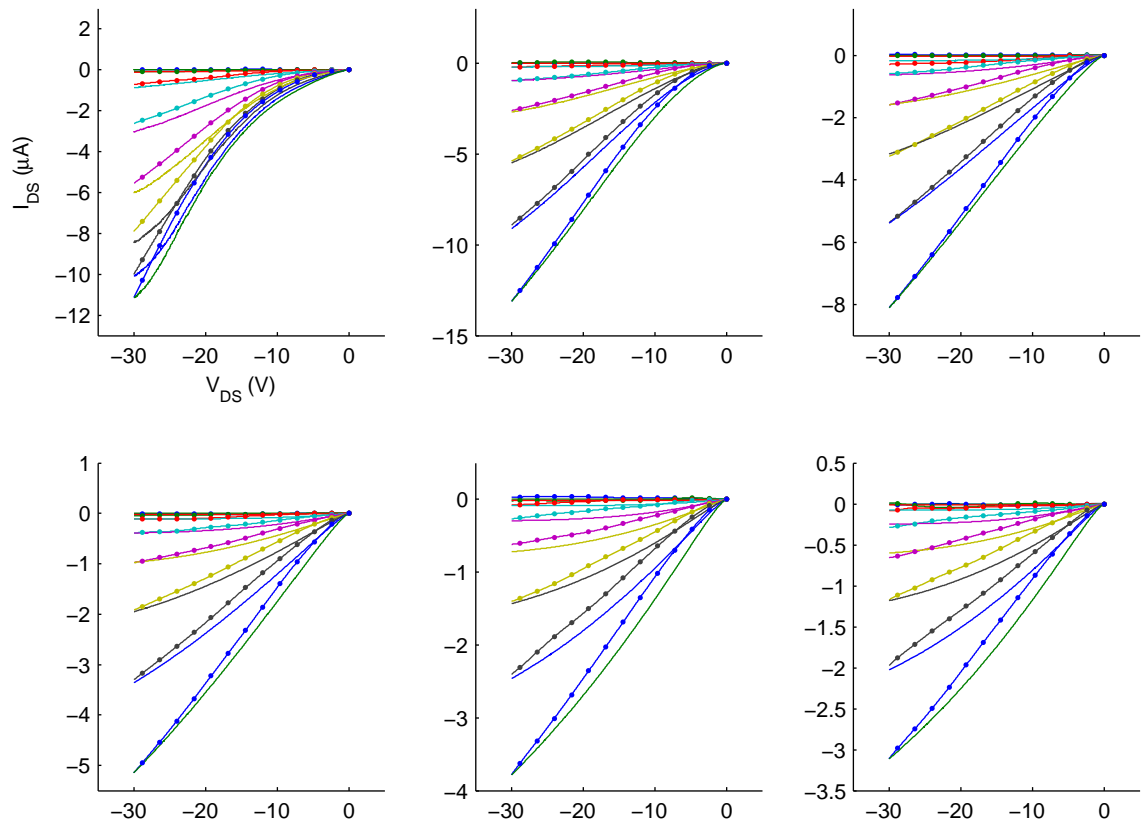
Figure 4.10 : Pt-injection at 1GHz. Dotted lines are integrated curves, smooth lines are the measured DC $I-V$ curves. The integrated curves are scaled to the maximum value in the DC curves, using a single scaling value. Top, from left to right: 1 μm, 5 μm, 10 μm. Bottom, from left to right: 15 μm, 20 μm, 25 μm. Gate voltage range in each plot is from 0V (top curve) to -70V (bottom curve).

P3HT. For shorter channel devices, the interpretation for the discrepancy is less clear. Additionally, for higher AC frequency, the correspondence between the integrated curves and DC transport curves improves for all channel lengths. The mechanism behind this behavior remains unclear.

Performing a second integration on the mixed-signal response yields fits worse than the ones presented in figures 4.7 through 4.10 and is not shown here. This method of analysis is suggestive, but by no means conclusive; clearly there is some merit to performing a single integration coupled with the interpretation that is associated with this method, but it fails to capture the entire breadth of the characteristics presented. Integrating the out-of-phase response similarly yields information that is not readily understandable, and has not been presented here. A more complete theoretical treatment is necessary in order to fully capture the experimental details presented here.

4.5   Conclusions

This chapter presents a novel method for probing P3HT (and other organic semi-conductors) at microwave frequencies with a low-frequency detection scheme. The original goal of this project was to attempt to infer high-frequency charge carrier information by twice integrating the detected signal. Data presented here shows a rich response of the organic semiconductor to various input frequencies and contact metals. Unfortunately, the interpretation of the data is incomplete as the expected method of analysis fails to produce results consistent with the theoretical model. Integrating the mixed-signal data once yields curves that look similar to measured DC $I-V$ curves, suggesting that mixing of the AC signal is occurring at the metal-organic interface, and not within the organic material, despite every attempt at making an Ohmic contact to P3HT. Despite the original purpose of this project, the technique devised here may be useful in characterizing the metal-organic interface in future organic semiconductor systems. To continue this work, a complete theoretical model

is required in order to fully explain the data and understand the interaction between P3HT, microwave frequencies, and contact metal work function.

Chapter 5

Final Remarks and Future Directions

In this thesis, the nature of the interaction between metals and conjugated materials - graphene and organic semiconductors - was investigated. The nature of organic semiconductors over a wide-range of temperatures was investigated, and it was found that both polymers and small-molecule OSCs transition from a thermally-activated hopping regime to a field-emission hopping regime as the temperature is decreased. Various other models were discussed that included exotic physics and insulator-to-metal transitions, but it was found that a theory-fit line is not sufficient evidence to claim the theory as an explanation for the data.

The nanometer-scale interaction between metals and graphene was also investigated. Graphene, a unique 2-dimensional carbon lattice, was suspended between gold and platinum electrodes with sub-50 nm spacing. At these length scales, platinum was found to donate mobile charge carriers into graphene, thus making it $p-$doped, whereas this did not occur for gold electrodes. As the separation between the electrodes increased, this disparity between gold and platinum disappeared and graphene returned to its bulk charge concentration values. From this, a rough estimate of the charge diffusion distance was estimated, and CVD-grown graphene films were characterized. This method illustrated a new way of making suspended graphene nanojunctions rapidly, and showed factors that need to be considered (like charge transfer hundreds of nanometers into the bulk) when engineering very small graphene devices.

Finally, a novel technique to characterize organic semiconductors was proposed. By using two microwave sources with one detuned from the other, and using the

organic field-effect transistor as a non-linear mixer, information about the high-frequency behavior of organic semiconductors could be extracted using inexpensive low-frequency detectors. This technique is still under development, and the analysis for the interactions between microwave signals and organic FETs is in its infancy. Nevertheless, this technique has potential in exploring the non-linear effects present in this system.

With graphene research growing at an exponential pace, and fundamental research on organic semiconductors slowing, it is natural to see the future direction of this work trending toward graphene. While few mysteries remain in organic semiconductor theory, their research potential is still high. Improving the mobility in organic semiconductors will remain an active area of research with promises of high-performance, flexible electronics in the near future. Interestingly, the commercial applications of graphene and OSCs currently overlap, with both being used (or attempting to be used) to fabricate transparent, low-power displays. These materials may also work well in tandem, perhaps by using graphene to improve charge mobility in OSCs. Anything said here about graphene is likely to be underway or complete by the time this is read... such is the nature of a hot research field. Graphene's potential to revolutionize condensed matter physics is not hyperbole - certainly, the Nobel Prize awarded to Andre Geim and Konstantin Novoselov in 2010 was well-deserved (if not, perhaps, slightly misplaced). It is truly an exciting time to be a physicist.

Bibliography

[1] Sarmalkar, V. Samsung Showcased AMOLED Display in CES 2011. *http://www.techienote.com/2010/12/samsung-showcased-amoled-display-in-ces-2011.html* (2010).

[2] Wesley. Samsung Unveils Flexible AMOLED Display. *http://www.futuretechlife.com/2011/01/30/samsung-unveils-flexible-amoled-display/* (2011).

[3] McAlpine, K. Theorists turn to graphene for clues to Higgs. *http://physicsworld.com/cws/article/news/2011/feb/01/theorists-turn-to-graphene-for-clues-to-higgs* (2011).

[4] Worne, J. H., Anthony, J. E. & Natelson, D. Transport in organic semiconductors in large electric fields: From thermal activation to field emission. *Appl. Phys. Lett.* **96**, 053308 (2010).

[5] Yuen, J. D., Menon, R., Coates, N. E., Namdas, E. B., Cho, S., Hannahs, S. T., Moses, D. & Heeger, A. J. Nonlinear transport in semiconducting polymers at high carrier densities. *Nat. Mater.* **8**, 572–575 (2009).

[6] Stolyarova, E., Rim, K. T., Ryu, S., Maultzsch, J., Kim, P., Brus, L. E., Heinz, T. F., Hybertsen, M. S. & Flynn, G. W. High-resolution scanning tunneling microscopy imaging of mesoscopic graphene sheets on an insulating surface. *Proc. Natl. Acad. Sci.* **104**, 9209–9212 (2007).

[7] Worne, J. H., Gullapalli, H., Galande, C., Ajayan, P. M. & Natelson, D. Local

charge transfer doping in suspended graphene nanojunctions. *Appl. Phys. Lett.* **100**, 023306 (2012).

[8] Giovannetti, G., Khomyakov, P., Brocks, G., Karpan, V., van den Brink, J. & Kelly, P. Doping Graphene with Metal Contacts. *Phys. Rev. Lett.* **101**, 026803 (2008).

[9] Natali, D. & Caironi, M. Charge Injection in Solution-Processed Organic Field-Effect Transistors: Physics, Models and Characterization Methods. *Adv. Mater.* **24**, 1357–1387 (2012).

[10] Mishra, A. & Bäuerle, P. Small molecule organic semiconductors on the move: promises for future solar energy technology. *Angewandte Chemie (International ed. in English)* **51**, 2020–2067 (2012).

[11] McGinness, J., Corry, P. & Proctor, P. Amorphous Semiconductor Switching in Melanins. *Science* **183**, 853–855 (1974).

[12] Shirakawa, H., Louis, E. & MacDiarmid, A. Synthesis of electrically conducting organic polymers: halogen derivatives of polyacetylene,(CH) x. *J. Chem. Soc., Chem.* 578–580 (1977).

[13] Bassler, H. Charge Transport in Disordered Organic Photoconductors. *Phys. Stat. Sol. B* **175**, 15–56 (1993).

[14] Nelson, J. Organic photovoltaic films. *Curr. Op. in Sol. State and Mat. Sci.* **6**, 87–95 (2002).

[15] Tanase, C., Meijer, E. J., Blom, P. W. M. & de Leeuw, D. M. Unification of the Hole Transport in Polymeric Field-Effect Transistors and Light-Emitting Diodes. *Phys. Rev. Lett.* **91**, 216601 (2003).

[16] Rubel, O., Baranovskii, S., Thomas, P. & Yamasaki, S. Concentration dependence of the hopping mobility in disordered organic solids. *Phys. Rev. B* **69**, 014206 (2004).

[17] Lonergan, M. Charge transport at conjugated polymer-inorganic semiconductor and conjugated polymer-metal interfaces. *Annu. Rev. Phys. Chem.* **55**, 257–298 (2004).

[18] Einstein, A., Podolsky, B. & Rosen, N. Can quantum-mechanical description of physical reality be considered complete? *Phys. Rev.* **47**, 777–780 (1935).

[19] Coropceanu, V., Cornil, J., da Silva Filho, D. A., Olivier, Y., Silbey, R. & Brédas, J.-L. Charge transport in organic semiconductors. *Chem. Rev.* **107**, 926–952 (2007).

[20] Tessler, N., Preezant, Y., Rappaport, N. & Roichman, Y. Charge Transport in Disordered Organic Materials and Its Relevance to Thin-Film Devices: A Tutorial Review. *Adv. Mater.* **21**, 2741–2761 (2009).

[21] Hamadani, B. H. & Natelson, D. Temperature-dependent contact resistances in high-quality polymer field-effect transistors. *Appl. Phys. Lett.* **84**, 443 (2004).

[22] Chen, J., Tee, C. K., Shtein, M., Martin, D. C. & Anthony, J. Controlled solution deposition and systematic study of charge-transport anisotropy in single crystal and single-crystal textured TIPS pentacene thin films. *Org. Elec.* **10**, 696–703 (2009).

[23] Sirringhaus, H., Brown, P. & Friend, R. Two-dimensional charge transport in self-organized, high-mobility conjugated polymers. *Nature* **401**, 685–688 (1999).

[24] Payne, M. M., Parkin, S. R., Anthony, J. E., Kuo, C.-c. & Jackson, T. N. Organic Field-Effect Transistors from Solution-Deposited Functionalized Acenes

with Mobilities as High as 1 cm^2 V^{-1} s^{-1}. *J. Am. Chem. Soc.* **127**, 4986–4987 (2005).

[25] Blom, P. W. M., de Jong, M. J. M. & van Munster, M. G. Electric-field and temperature dependence of the hole mobility in poly(p-phenylene vinylene). *Phys. Rev. B* **55**, 656–659 (1997).

[26] Sirringhaus, H. Device Physics of Solution-Processed Organic Field-Effect Transistors. *Adv. Mater.* **17**, 2411–2425 (2005).

[27] Le Comber, P. G. & Spear, W. E. Electronic transport in amorphous silicon films. *Phys. Rev. Lett.* **25**, 1968–1970 (1970).

[28] Horowitz, G. & Hajlaoui, M. E. Mobility in Polycrystalline Oligothiophene Field-Effect Transistors Dependent on Grain Size. *Adv. Mater.* **12**, 1046–1050 (2000).

[29] Podzorov, V., Sysoev, S. E., Loginova, E., Pudalov, V. M. & Gershenson, M. E. Single-crystal organic field effect transistors with the hole mobility 8 cm^2 V^{-1} s^{-1}. *Appl. Phys. Lett.* **83**, 3504–3506 (2003).

[30] Anthony, J. E. Functionalized acenes and heteroacenes for organic electronics. *Chem. Rev.* **106**, 5028–5048 (2006).

[31] Ostroverkhova, O., Cooke, D. G., Hegmann, F. A., Anthony, J. E., Podzorov, V., Gershenson, M. E., Jurchescu, O. D. & Palstra, T. T. M. Ultrafast carrier dynamics in pentacene, functionalized pentacene, tetracene, and rubrene single crystals. *Appl. Phys. Lett.* **88**, 162101 (2006).

[32] Park, S. K., Jackson, T. N., Anthony, J. E. & Mourey, D. A. High mobility solution processed 6,13-bis(triisopropyl-silylethynyl) pentacene organic thin film transistors. *Appl. Phys. Lett.* **91**, 063514 (2007).

[33] Sundar, V. C., Zaumseil, J., Podzorov, V., Menard, E., Willett, R. L., Someya, T., Gershenson, M. E. & Rogers, J. A. Elastomeric transistor stamps: reversible probing of charge transport in organic crystals. *Science* **303**, 1644–1646 (2004).

[34] De Renzi, V., Rousseau, R., Marchetto, D., Biagi, R., Scandolo, S. & del Pennino, U. Metal Work-Function Changes Induced by Organic Adsorbates: A Combined Experimental and Theoretical Study. *Phys. Rev. Lett.* **95**, 046804 (2005).

[35] Campbell, I. H., Rubin, S., Zawodzinski, T. A., Kress, J. D., Martin, R. l., Smith, D. l., Barashkov, N. N. & Ferraris, J. P. Controlling Schottky energy barriers in organic electronic devices using self-assembled monolayers. *Phys. Rev. B* **54**, 14321–14324 (1996).

[36] Nüesch, F., Rotzinger, F., Si-Ahmed, L. & Zuppirolo, L. Chemical potential shifts at organic device electrodes induced by grafted monolayers. *Chem. Phys. Lett.* **288**, 861–867 (1998).

[37] Hamadani, B. H., Corley, D. a., Ciszek, J. W., Tour, J. M. & Natelson, D. Controlling charge injection in organic field-effect transistors using self-assembled monolayers. *Nano Lett.* **6**, 1303–1306 (2006).

[38] Worne, J. H., Giridharagopal, R., Kelly, K. F. & Natelson, D. Interfacial charge transfer in nanoscale polymer transistors. *Nano Res.* **1**, 341–350 (2008).

[39] Ng, T. N., Silveira, W. R. & Marohn, J. A. Dependence of Charge Injection on Temperature, Electric Field, and Energetic Disorder in an Organic Semiconductor. *Phys. Rev. Lett.* **98**, 066101 (2007).

[40] Silveira, W. R. & Marohn, J. A. Microscopic View of Charge Injection in an Organic Semiconductor. *Phys. Rev. Lett.* **93**, 116104 (2004).

[41] Sze, S. M. & Ng, K. K. *Physics of Semiconductor Devices* (Wiley-VCH, Hoboken, NJ, 2007), 3rd edn.

[42] Scott, J. C. Metal-organic interface and charge injection in organic electronic devices. *J. Vac. Sci. Tech. A* **21**, 521 (2003).

[43] Hill, I. G., Rajagopal, A. & Kahn, A. Molecular level alignment at organic semiconductor-metal interfaces. *Appl. Phys. Lett.* **73**, 662–664 (1998).

[44] Ishii, H. & Seki, K. Energy Level Alignment at Organic/Metal Interfaces Studied by UV Photoemission: Breakdown of Traditional Assumption of a Common Vacuum Level at the Interface. *IEEE T. Electron. Dev.* **44**, 1295–1301 (1997).

[45] Rajagopal, A., Wu, C. I. & Kahn, A. Energy level offset at organic semiconductor heterojunctions. *J. Appl. Phys.* **83**, 2649–2655 (1998).

[46] Tengstedt, C., Osikowicz, W., Salaneck, W. R., Parker, I. D., Hsu, C.-H. & Fahlman, M. Fermi-level pinning at conjugated polymer interfaces. *Appl. Phys. Lett.* **88**, 053502 (2006).

[47] Crispin, A., Crispin, X., Fahlman, M., Berggren, M. & Salaneck, W. R. Transition between energy level alignment regimes at a low band gap polymer-electrode interfaces. *Appl. Phys. Lett.* **89**, 213503 (2006).

[48] Koch, N. & Vollmer, A. Electrode-molecular semiconductor contacts: Work-function-dependent hole injection barriers versus Fermi-level pinning. *Appl. Phys. Lett.* **89**, 162107 (2006).

[49] Hamadani, B. H., Ding, H., Gao, Y. & Natelson, D. Doping-dependent charge injection and band alignment in organic field-effect transistors. *Phys. Rev. B* **72**, 235302 (2005).

[50] Mermin, N. Crystalline order in two dimensions. *Phys. Rev.* **176**, 250–254 (1968).

[51] Novoselov, K. S., Jiang, D., Schedin, F., Booth, T. J., Khotkevich, V. V., Morozov, S. V. & Geim, a. K. Two-dimensional atomic crystals. *Proc. Natl. Acad. Sci.* **102**, 10451–10453 (2005).

[52] Meyer, J. C., Geim, A. K., Katsnelson, M. I., Novoselov, K. S., Booth, T. J. & Roth, S. The structure of suspended graphene sheets. *Nature* **446**, 60–63 (2007).

[53] Castro Neto, A. H., Peres, N. M. R., Novoselov, K. S. & Geim, A. K. The electronic properties of graphene. *Rev. Mod. Phys.* **81**, 109–162 (2009).

[54] Hsieh, D., Qian, D., Wray, L., Xia, Y., Hor, Y. S., Cava, R. J. & Hasan, M. Z. A topological Dirac insulator in a quantum spin Hall phase. *Nature* **452**, 970–974 (2008).

[55] Geim, A. K. & Novoselov, K. S. The rise of graphene. *Nat. Mater.* **6**, 183–191 (2007).

[56] Du, X., Skachko, I., Barker, A. & Andrei, E. Y. Approaching ballistic transport in suspended graphene. *Nat. Nano.* **3**, 491–495 (2008).

[57] Chen, J.-H., Jang, C., Adam, S., Fuhrer, M. S., Williams, E. D. & Ishigami, M. Charged-impurity scattering in graphene. *Nat. Phys.* **4**, 377–381 (2008).

[58] Novoselov, K. S., Geim, A. K., Morozov, S. V., Jiang, D., Katsnelson, M. I., Grigorieva, I. V., Dubonos, S. V. & Firsov, A. A. Two-dimensional gas of massless Dirac fermions in graphene. *Nature* **438**, 197–200 (2005).

[59] Martin, J., Akerman, N., Ulbricht, G., Lohmann, T., Smet, J. H., von Klitzing, K. & Yacoby, A. Observation of electron-hole puddles in graphene using a scanning single-electron transistor. *Nat. Phys.* **4**, 144–148 (2007).

[60] Tan, Y.-W., Zhang, Y., Bolotin, K., Zhao, Y., Adam, S., Hwang, E. H., Das Sarma, S., Stormer, H. L. & Kim, P. Measurement of Scattering Rate and Minimum Conductivity in Graphene. *Phys. Rev. Lett.* **99**, 246803 (2007).

[61] Avouris, P. Graphene: Electronic and Photonic Properties and Devices. *Nano Lett.* **10**, 4285–4294 (2010).

[62] Yu, Q., Jauregui, L. A., Wu, W., Colby, R., Tian, J., Su, Z., Cao, H., Liu, Z., Pandey, D., Wei, D., Chung, T. F., Peng, P., Guisinger, N. P., Stach, E. A., Bao, J., Pei, S.-S. & Chen, Y. P. Control and characterization of individual grains and grain boundaries in graphene grown by chemical vapour deposition. *Nat. Mater.* **10**, 443–449 (2011).

[63] Scheinert, S. & Paasch, G. Interdependence of contact properties and field- and density-dependent mobility in organic field-effect transistors. *J. Appl. Phys.* **105**, 014509 (2009).

[64] Pasveer, W., Cottaar, J., Tanase, C., Coehoorn, R., Bobbert, P., Blom, P. W. M., de Leeuw, D. & Michels, M. Unified Description of Charge-Carrier Mobilities in Disordered Semiconducting Polymers. *Phys. Rev. Lett.* **94**, 206601 (2005).

[65] Hamadani, B. H., Richter, C. A., Gundlach, D. J., Kline, R. J., Mcculloch, I. & Heeney, M. Influence of source-drain electric field on mobility and charge transport in organic field-effect transistors. *J. Appl. Phys.* **102**, 044503 (2007).

[66] Frenkel, J. On Pre-Breakdown Phenomena in Insulators and Electronic Semi-Conductors. *Phys. Rev.* **54**, 647–648 (1938).

[67] Dhoot, A., Wang, G., Moses, D. & Heeger, A. Voltage-Induced Metal-Insulator Transition in Polythiophene Field-Effect Transistors. *Phys. Rev. Lett.* **96**, 246403 (2006).

[68] Bockrath, M., Cobden, D., Lu, J. & Rinzler, A. Luttinger-liquid behaviour in carbon nanotubes. *Nature* **397**, 598–601 (1999).

[69] Yacoby, A., Stormer, H., Wingreen, N., Pfeiffer, L., Baldwin, K. & West, K. Nonuniversal Conductance Quantization in Quantum Wires. *Phys. Rev. Lett.* **77**, 4612–4615 (1996).

[70] Prigodin, V. N. & Epstein, A. J. Comment on "Voltage-Induced Metal-Insulator Transition in Polythiophene Field-Effect Transistors". *Phys. Rev. Lett.* **98**, 259703 (2007).

[71] Larkin, A. & Khmelnitski, D. E. Activation conductivity in disordered systems with large localization length. *Soviet Physics JETP* **56**, 647 (1982).

[72] Shklovskii, B. I. Hopping Conduction in Semiconductors Subject to a Strong Electric Field. *Sov. Phys. Semicond.* **6**, 1964 (1973).

[73] Wei, J. H., Gao, Y. L. & Wang, X. R. Inverse square-root field dependence of conductivity in organic field-effect transistors. *Appl. Phys. Lett.* **94**, 073301 (2009).

[74] Haddon, R. C., Chi, X., Itkis, M. E., Anthony, J. E., Eaton, D. L., Siegrist, T., Mattheus, C. C. & Palstra, T. T. M. Band Electronic Structure of One- and Two-Dimensional Pentacene Molecular Crystals. *Mol. Crys.* **106**, 8288–8292 (2002).

[75] McCullough, R. D., Lowe, R. D., Jayaraman, M. & Anderson, D. L. Design, synthesis, and control of conducting polymer architectures: structurally homogeneous poly(3-alkylthiophenes). *J. Org. Chem.* **58**, 904–912 (1993).

[76] McCulloch, I., Heeney, M., Bailey, C., Genevicius, K., Macdonald, I., Shkunov, M., Sparrowe, D., Tierney, S., Wagner, R., Zhang, W., Chabinyc, M. L., Kline,

R. J., McGehee, M. D. & Toney, M. F. Liquid-crystalline semiconducting polymers with high charge-carrier mobility. *Nat. Mater.* **5**, 328–333 (2006).

[77] Hamadani, B. H., Gundlach, D. J., McCulloch, I. & Heeney, M. Undoped polythiophene field-effect transistors with mobility of 1 cm² V⁻¹ s⁻¹. *Appl. Phys. Lett.* **91**, 243512 (2007).

[78] Aleshin, A. N., Lee, H. J., Park, Y. W. & Akagi, K. One-Dimensional Transport in Polymer Nanofibers. *Phys. Rev. Lett.* **93**, 196601 (2004).

[79] Liao, L., Lin, Y.-C., Bao, M., Cheng, R., Bai, J., Liu, Y., Qu, Y., Wang, K. L., Huang, Y. & Duan, X. High-speed graphene transistors with a self-aligned nanowire gate. *Nature* **467**, 305–308 (2010).

[80] Mueller, T., Xia, F. & Avouris, P. Graphene photodetectors for high-speed optical communications. *Nat. Phot.* **4**, 297–301 (2010).

[81] Geim, A. K. Graphene: status and prospects. *Science* **324**, 1530–1534 (2009).

[82] Sabio, J., Seoánez, C., Fratini, S., Guinea, F., Neto, a. & Sols, F. Electrostatic interactions between graphene layers and their environment. *Phys. Rev. B* **77**, 195409 (2008).

[83] Dean, C. R., Young, A. F., Meric, I., Lee, C., Wang, L., Sorgenfrei, S., Watanabe, K., Taniguchi, T., Kim, P., Shepard, K. L. & Hone, J. Boron nitride substrates for high-quality graphene electronics. *Nat. Nano.* **5**, 722–726 (2010).

[84] Lui, C. H., Liu, L., Mak, K. F., Flynn, G. W. & Heinz, T. F. Ultraflat graphene. *Nature* **462**, 339–341 (2009).

[85] Wang, X., Li, X., Zhang, L., Yoon, Y., Weber, P. K., Wang, H., Guo, J. & Dai, H. N-doping of graphene through electrothermal reactions with ammonia. *Science* **324**, 768–771 (2009).

[86] Wehling, T. O., Novoselov, K. S., Morozov, S. V., Vdovin, E. E., Katsnelson, M. I., Geim, A. K. & Lichtenstein, A. I. Molecular doping of graphene. *Nano Lett.* **8**, 173–177 (2008).

[87] Lee, E. J. H., Balasubramanian, K., Weitz, R. T., Burghard, M. & Kern, K. Contact and edge effects in graphene devices. *Nat. Nano.* **3**, 486–490 (2008).

[88] Mueller, T., Xia, F., Freitag, M., Tsang, J. & Avouris, P. Role of contacts in graphene transistors: A scanning photocurrent study. *Phys. Rev. B* **79**, 245430 (2009).

[89] Sundaram, R. S., Gomez-Navarro, C., Lee, E. J. H., Burghard, M. & Kern, K. Noninvasive metal contacts in chemically derived graphene devices. *Appl. Phys. Lett.* **95**, 223507 (2009).

[90] Blake, P., Yang, R., Morozov, S., Schedin, F., Ponomarenko, L., Zhukov, A., Nair, R., Grigorieva, I., Novoselov, K. & Geim, A. Influence of metal contacts and charge inhomogeneity on transport properties of graphene near the neutrality point. *Solid State Commun.* **149**, 1068–1071 (2009).

[91] Huard, B., Stander, N., Sulpizio, J. & Goldhaber-Gordon, D. Evidence of the role of contacts on the observed electron-hole asymmetry in graphene. *Phys. Rev. B* **78**, 121402 (2008).

[92] Golizadeh-Mojarad, R. & Datta, S. Effect of contact induced states on minimum conductivity in graphene. *Phys. Rev. B* **79**, 085410 (2009).

[93] Lang, N. D. & Avouris, P. Carbon-atom wires: charge-transfer doping, voltage drop, and the effect of distortions. *Phys. Rev. Lett.* **84**, 358–361 (2000).

[94] Petit, P. Tuning and monitoring the electronic structure of carbon nanotubes. *Chem. Phys. Lett.* **305**, 370–374 (1999).

[95] Rao, A. M., Eklund, P. C., Bandow, S. & Thess, A. Evidence for charge transfer in doped carbon nanotube bundles from Raman scattering. *Nature* **191**, 257–259 (1997).

[96] Khomyakov, P. A., Giovannetti, G., Rusu, P. C., Brocks, G., van den Brink, J. & Kelly, P. J. First-principles study of the interaction and charge transfer between graphene and metals. *Phys. Rev. B* **79**, 1–12 (2009).

[97] Jalilian, R., Jauregui, L. A., Lopez, G., Tian, J., Roecker, C., Yazdanpanah, M. M., Cohn, R. W., Jovanovic, I. & Chen, Y. P. Scanning gate microscopy on graphene: charge inhomogeneity and extrinsic doping. *Nanotechnology* **22**, 295705 (2011).

[98] Varykhalov, A., Scholz, M., Kim, T. & Rader, O. Effect of noble-metal contacts on doping and band gap of graphene. *Phys. Rev. B* **82**, 121101 (2010).

[99] Fursina, A., Lee, S., Sofin, R. G. S., Shvets, I. V. & Natelson, D. Nanogaps with very large aspect ratios for electrical measurements. *Appl. Phys. Lett.* **92**, 113102 (2008).

[100] Li, X., Cai, W., An, J., Kim, S., Nah, J., Yang, D., Piner, R., Velamakanni, A., Jung, I., Tutuc, E., Banerjee, S. K., Colombo, L. & Ruoff, R. S. Large-area synthesis of high-quality and uniform graphene films on copper foils. *Science* **324**, 1312–1314 (2009).

[101] Ferrari, A. C., Meyer, J. C., Scardaci, V., Casiraghi, C., Lazzeri, M., Mauri, F., Piscanec, S., Jiang, D., Novoselov, K. S., Roth, S. & Geim, a. K. Raman Spectrum of Graphene and Graphene Layers. *Phys. Rev. Lett.* **97**, 187401 (2006).

[102] Checkelsky, J. G., Li, L. & Ong, N. P. Zero-Energy State in Graphene in a High Magnetic Field. *Phys. Rev. Lett.* **100**, 206801 (2008).

[103] Katsnelson, M. I. & Geim, A. K. Electron scattering on microscopic corrugations in graphene. *Phil. Trans. R. Soc. A* **366**, 195–204 (2008).

[104] McCreary, K. M., Pi, K. & Kawakami, R. K. Metallic and insulating adsorbates on graphene. *Appl. Phys. Lett.* **98**, 192101 (2011).

[105] Nouchi, R., Saito, T. & Tanigaki, K. Determination of Carrier Type Doped from Metal Contacts to Graphene by Channel-Length-Dependent Shift of Charge Neutrality Points. *Appl. Phys. Exp.* **4**, 035101 (2011).

[106] Scheinert, S. & Paasch, G. Fabrication and analysis of polymer field-effect transistors. *Phys. Stat. Sol. A* **201**, 1263–1301 (2004).

[107] Arkhipov, V. I., Wolf, U. & Bassler, H. Current injection from a metal to a disordered hopping system. II. Comparison between analytic theory and simulation. *Phys. Rev. B* **59**, 7514–7520 (1999).

[108] Schmechel, R. & von Seggern, H. Electronic traps in organic transport layers. *Phys. Stat. Sol. A* **201**, 1215–1235 (2004).

[109] Basu, D. & Dodabalapur, A. Drift Velocity and Drift Mobility Measurement. *Adv. Polym. Sci.* **223**, 73–112 (2010).

[110] v Laarhoven, H. A., Flipse, C. F. J., Koeberg, M., Bonn, M., Hendry, E., Orlandi, G., Jurchescu, O. D., Palstra, T. T. M. & Troisi, A. On the mechanism of charge transport in pentacene. *J. Chem. Phys.* **129**, 044704 (2008).

[111] Cantatore, E., Geuns, T. C. T., Gelinck, G. H., van Veenendaal, E., Gruijthuijsen, A. F. A., Schrijnemakers, L., Drews, S. & de Leeuw, D. M. A 13.56-MHz RFID System Based on Organic Transponders. *IEEE J. Solid-St. Circ.* **42**, 84–92 (2007).

[112] Steudel, S., De Vusser, S., Myny, K., Lenes, M., Genoe, J. & Heremans, P. Comparison of organic diode structures regarding high-frequency rectification behavior in radio-frequency identification tags. *J. Appl. Phys.* **99**, 114519 (2006).

[113] Baude, P. F., Ender, D. A., Haase, M. a., Kelley, T. W., Muyres, D. V. & Theiss, S. D. Pentacene-based radio-frequency identification circuitry. *Appl. Phys. Lett.* **82**, 3964–3966 (2003).

[114] Rotzoll, R., Mohapatra, S., Olariu, V., Wenz, R., Grigas, M., Dimmler, K., Shchekin, O. & Dodabalapur, A. Radio frequency rectifiers based on organic thin-film transistors. *Appl. Phys. Lett.* **88**, 123502 (2006).

[115] Steudel, S., Myny, K., Arkhipov, V., Deibel, C., De Vusser, S., Genoe, J. & Heremans, P. 50 MHz rectifier based on an organic diode. *Nat. Mater.* **4**, 597–600 (2005).

[116] Hoppe, A., Balster, T., Muck, T. & Wagner, V. Scaling limits and MHz operation in thiophene-based field-effect transistors. *Phys. Stat. Sol. A* **205**, 612–625 (2008).

[117] Lenski, D. R., Southard, A. & Fuhrer, M. S. Frequency-dependent complex conductivity of an organic thin-film transistor. *Appl. Phys. Lett.* **94**, 232103 (2009).

[118] Obrzut, J. & Page, K. A. Electrical conductivity and relaxation in poly(3-hexylthiophene). *Phys. Rev. B* **80**, 195211 (2009).

[119] Martens, H., Brom, H. & Blom, P. W. M. Frequency-dependent electrical response of holes in poly (p-phenylene vinylene). *Phys. Rev. B* **60**, 8489–8492 (1999).

[120] Giridharagopal, R., Zhang, J. & Kelly, K. F. Antenna-based ultrahigh vacuum

microwave frequency scanning tunneling microscopy system. *Rev. Sci. Instrum.* **82**, 053710 (2011).

[121] Hamadani, B. H. & Natelson, D. Nonlinear charge injection in organic field-effect transistors. *J. Appl. Phys.* **97**, 064508 (2005).

[122] Hamadani, B. H. & Natelson, D. Extracting Contact Effects in Organic FETs. *Proc. IEEE* **93**, 1306–1311 (2005).